Frequency Combs for Spectroscopy in the Vacuum Ultraviolet

by

David R. Carlson

A Dissertation Submitted to the Faculty of the

College of Optical Sciences

In Partial Fulfillment of the Requirements

For the Degree of

Doctor of Philosophy

In the Graduate College

The University of Arizona

2 0 1 6

The University of Arizona

Graduate College

As members of the Dissertation Committee, we certify that we have read the dissertation prepared by David R. Carlson, titled Frequency Combs for Spectroscopy in the Vacuum Ultraviolet and recommend that it be accepted as fulfilling the dissertation requirement for the Degree of Doctor of Philosophy.

_____ Date: 4/20/16

R. Jason Jones

_____ Date: 4/20/16

Brian Anderson

_____ Date: 4/20/16

Ewan Wright

Final approval and acceptance of this dissertation is contingent upon the candidates submission of the final copies of the dissertation to the Graduate College.

I hereby certify that I have read this dissertation prepared under my direction and recommend that it be accepted as fulfilling the dissertation requirement.

_____ Date: 4/20/16

Dissertation Director: R. Jason Jones

Statement by Author

This dissertation has been submitted in partial fulfillment of requirements for an advanced degree at The University of Arizona and is deposited in the University Library to be made available to borrowers under rules of the Library.

Brief quotations from this dissertation are allowable without special permission, provided that an accurate acknowledgement of the source is made. Requests for permission for extended quotation from or reproduction of this manuscript in whole or in part may be granted by the head of the major department or the Dean of the Graduate College when in his or her judgment the proposed use of the material is in the interests of scholarship. In all other instances, however, permission must be obtained from the author.

SIGNED: David Carlson

Acknowledgments

During my time as a graduate student I have had the privilege of meeting and working with many capable, energetic, and fun people whose support has helped make this dissertation possible. I would especially like to thank my advisor Jason Jones for his guidance and scientific insight. My time working in his lab has been a great experience and I am grateful for the opportunity. I also want to acknowledge the other members of my committee, Ewan Wright and Brian Anderson, for taking the time to provide feedback on this dissertation.

I want to thank my lab mates Tsung-Han Wu, Jane Lee, Justin Paul, and Christian Lytle for their work on the experiment, teaching me new skills, and many helpful discussions over the past several years. Also, some of the numerical simulations included here were done with the help of two other students, John Mongelli and Gregory Jacob.

When I first came to Tucson, I joined the the U of A Cycling Team and got involved in bike racing. Training and racing with all of my friends on the team has been one of the highlights of my time in graduate school and has provided a good balance with work in the lab.

Finally, I would like to acknowledge the support of my family, especially my parents and my wife Cécile, who have always encouraged me in the things I do. I can't imagine being at this point without their love, patience, and trust.

Table of Contents

Table of Contents—*Continued*

Abstract

This dissertation explores frequency comb spectroscopy and, in particular, its extension to the vacuum-ultraviolet (VUV) and extreme-ultraviolet (XUV) wavelength regimes through a technique called intracavity high harmonic generation (IHHG). By combining the techniques of passive pulse amplification in an enhancement cavity with high harmonic generation, IHHG enables the direct conversion of near-infrared radiation to the VUV/XUV while still maintaining the underlying comb structure.

As part of this work, a series of numerical simulations was performed to investigate the plasma that is formed in the IHHG process and its implications for the resulting VUV comb. It was demonstrated that a fundamental limitation to the performance of IHHG experiments is due to the single-pass ionization phase shift acquired by the pulse circulating in the enhancement cavity. Furthermore, we showed that a static background plasma accumulates between pulses and complicates cavity stabilization.

Insights gained from the simulations led to the development of a novel pump-probe technique using the enhancement cavity that allowed a direct measurement of the intracavity plasma and its decay dynamics in real-time. Because the plasma lifetime plays such a crucial role in the operation of these cavities, it was important to have a method to test ways of reducing it.

To build on our initial IHHG results showing record-level powers in the XUV, we implemented a fully phase-coherent dual comb spectrometer consisting of two identical IHHG systems operating in parallel. The system is designed for precision spectroscopy in the VUV and is based on a pair of homemade ytterbium fiber lasers that use a parabolic amplification scheme to achieve 80 fs pulses after amplification to 50 W of average power. Initial dual comb data showing system performance at the fundamental frequency and third harmonic are presented.

Chapter 1

Introduction

The field of precision metrology made a dramatic leap forward with the invention of the optical frequency comb which provided, for the first time, a direct link between optical frequencies and radio frequency (RF) instrumentation. Before this link, it was next to impossible to directly measure the optical frequency of a laser. While there were some initial demonstrations showing the potential of frequency combs as early as the late 1970s [1, 2], it wasn't until the late 1990s that mode-locked laser technology had advanced enough to create a true frequency comb composed of a million discrete comb lines over a broad spectral bandwidth [3, 4].

In 2005, half of the Nobel Prize in physics was awarded to Theodor Hänsch and John Hall for their pioneering work on frequency combs. The development of combs over the past 15 years has led to advances in atomic frequency standards [5, 6], precision spectroscopy [7], laser ranging and remote sensing [8], fundamental physics [9], biological engineering [10], and astronomy [11, 12]. Figure 1.1 shows that, despite their success, the spectral range covered by these combs has largely been restricted to optical, near-infrared, and more recently, mid-infrared wavelengths [13].

Extending comb technology to the vacuum-ultraviolet (VUV, 100-200 nm) and extreme-ultraviolet (XUV, 10-100 nm) spectral regions will enable similar advances in a traditionally challenging-to-reach part of the electromagnetic spectrum. There is significant interest in doing so, in part, because many well-studied atomic systems have their first ground state transitions in this wavelength range. One such example is the hydrogen-like helium ion (He^+) whose 1S-2S transition lies in the XUV near 61 nm. Accurate measurement of this transition in He^+ will allow for more stringent tests

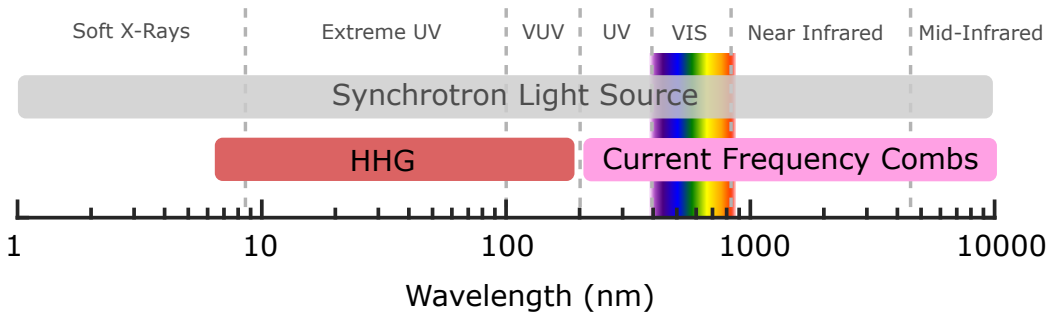

FIGURE 1.1. Range of electromagnetic spectrum covered by current-generation frequency combs. High harmonic generation (HHG) provides a way to extend this range to the VUV and XUV wavelength regimes that are currently only accesible with synchrotron sources.

of quantum electrodynamics and improve the search for variations in fundamental physical constants [14].

Another example relating to testing the limits of physical theories concerns the search for variation in the fine structure constant α over time. This is accomplished by comparing atomic transition frequencies on earth to those observed in spectra obtained from distant quasars. However, most relevant transitions are in the VUV and XUV and thus the current experiments have been limited by the achievable frequency resolution of the laboratory light sources [15].

Another promising application for a VUV frequency comb is the possibility of direct laser-excitation of a magnetic dipole transition in the nucleus of ^{229}Th. This particular isotope of thorium is unique in that it has a very low-lying nuclear excited state transition near $\lambda = 150$ nm [16]. By doping a CaF_2 crystal with ^{229}Th it may be possible to excite this transition with a VUV comb and use it to create the next generation of ultra-stable frequency standards [17].

Performing high precision spectroscopic measurements in the VUV/XUV is a challenging task due to the difficulty of creating a suitable light source. Synchrotron sources can provide access to these wavelengths at a very high photon flux but are

limited in their frequency resolution and require extremely large and expensive facilities to operate [18, 19]. Nevertheless, in 2011 a Fourier transform spectroscopy experiment on the DESIRS VUV beamline at the SOLEIL synchrotron in France recorded a high-resolution (6×10^6 resolving power) absorption spectrum of krypton over the 40-250 nm wavelength range [18]. While an improvement over dispersive spectrometers, the resolution is still many orders of magnitude lower than what is possible with well-stabilized optical frequency combs.

An alternative to synchrotron sources is called high harmonic generation (HHG) and offers a table-top means of reaching the VUV/XUV through frequency up-conversion. Traditional HHG systems are based on a high power, low repetition rate, pulsed IR laser that allows very high pulse energies and peak intensities. However, the low repetition rate of these lasers means that the delay between pulses is too large to maintain the pulse-to-pulse coherence required for a frequency comb. One HHG-based approach to XUV spectroscopy involves amplifying a single pulse pair from the output of a near-IR frequency comb. Excitation of an atomic transition by this pulse pair produces a cosine-modulated signal that can be used to extract the transition frequency. This technique has been demonstrated at 51 nm in helium at an optical resolution of 6 MHz [20]. While this represented a significant improvement over earlier results, the full resolution of the source frequency comb was not utilized since only two pulses were used in the HHG conversion.

The first true demonstration of XUV frequency comb spectroscopy was demonstrated in 2012 by Cingoz et. al [21]. Their system was also based on HHG but the harmonic generation was performed inside a high-finesse optical cavity in order to maintain high pulse energies at the full repetition rate of the original frequency comb[1]. This direct frequency comb approach was used to probe transitions at 82 nm in argon and at 63 nm in neon and demonstrated that the cavity-based HHG tech-

[1]This technique is called "intracavity high harmonic generation" (IHHG) and forms the basis of the system used in this thesis. A detailed description of IHHG is provided in Chapter 3

nique has matured enough to perform useful spectroscopic measurements. However, due to limitations with using a single frequency comb, the system could only probe very narrow, isolated, atomic transitions.

In this dissertation, a similar light source for spectroscopy in the VUV using two frequency combs is described and results presented for both numerical and experimental investigations into its capabilities and limitations. Chapter 2 introduces the key theoretical concepts of both frequency combs and high harmonic generation while Chapter 3 merges these concepts to demonstrate intracavity high harmonic generation (IHHG) as a means of creating frequency combs in the VUV/XUV. The experimental system used and the results obtained to date are also presented in this section. Chapter 4 addresses some of the limitations of the IHHG technique and presents results from both simulations and direct measurements of the enhancement cavity dynamics. The extension of dual comb spectroscopy to the VUV is described in Chapter 5 and initial results are shown. Finally, Chapter 6 includes some concluding remarks and briefly discusses the outlook of this field of study.

Chapter 2

Theoretical Background

2.1 Frequency Combs

2.1.1 Basic Principles

A frequency comb is formed from the output of a stabilized mode-locked laser. In the time domain, this is represented by an infinite train of evenly spaced ultrashort pulses with a well-defined phase relationship between pulses. To understand how this train of pulses becomes a "comb" in the frequency domain, it is instructive to follow the progression shown in Figure 2.1. A single ultrashort pulse, with a Gaussian temporal profile, produces a smooth Gaussian-shaped spectral profile with a full width at half maximum (FWHM) of $\Delta\nu$ proportional to $1/\Delta t$, where Δt is the FWHM pulse duration. If a second identical pulse follows the first after a time T, then a cosine-modulated series of fringes with period $1/T$ is visible under the single-pulse spectral envelope. Subsequent pulses delayed by T produce a spectral interference pattern that yields sharp peaks separated by the same $1/T$ spacing. For an essentially infinite train of pulses at repetition frequency $f_{\text{rep}} = 1/T$, these peaks become extremely narrow and form the "teeth" of the frequency comb.

In the time domain picture shown in Figure 2.2, it is possible to have a phase shift between the electric field carrier frequency and the pulse envelope from pulse to pulse that arises from a difference in the group and phase velocities. This shift, $\Delta\phi$, produces an offset of the frequency comb lines $f_{\text{ceo}} = f_{\text{rep}}\Delta\phi/2\pi$. Since both f_{rep} and f_{ceo} are frequencies in the RF domain that can be measured directly, knowledge of

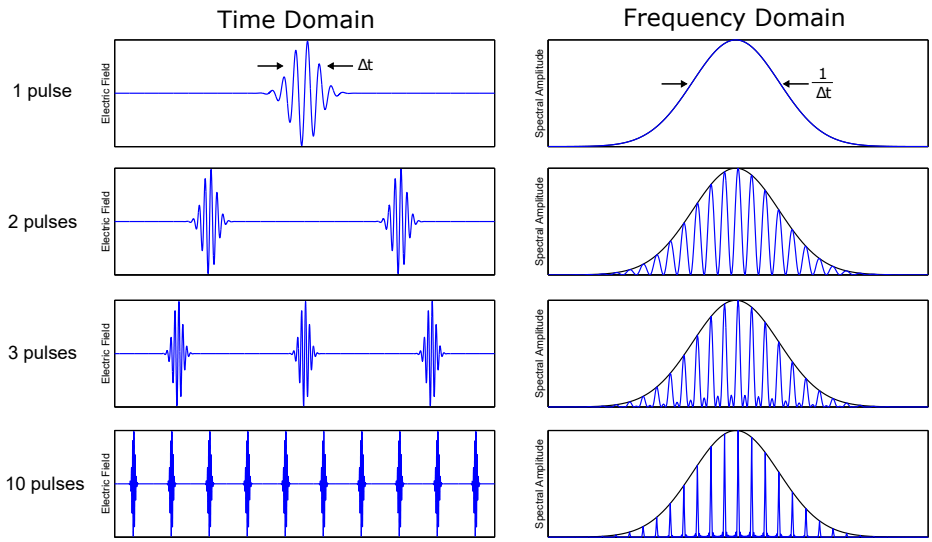

FIGURE 2.1. Progression showing how a series of phase coherent pulses in time leads to a "comb" of well-resolved peaks in the frequency domain. The overall spectral envelope is determined by the frequency spectrum of an isolated pulse.

their values allows precise determination of the optical comb frequencies.

In the frequency domain, the comb structure is described simply by

$$\nu_m = f_{\text{ceo}} + m f_{\text{rep}} \tag{2.1}$$

where ν_m is the optical frequency of the m^{th} comb mode. Figure 2.3 provides a visual representation of this equation showing the link between optical frequencies and the RF components f_{ceo} and f_{rep}.

The laser repetition rate can be detected easily by observing the pulse train with a fast photodiode and can be stabilized relative to a high quality RF reference. Detection and stabilization of the carrier-envelope offset frequency is more difficult, but it is critical for frequency applications requiring precise knowledge of the comb modes as well as for time domain applications where the pulse-to-pulse reproducibility of the electric field phase is important. A self-referencing technique requiring an octave-spanning comb is the most common method of detecting f_{ceo} [4, 22]. An

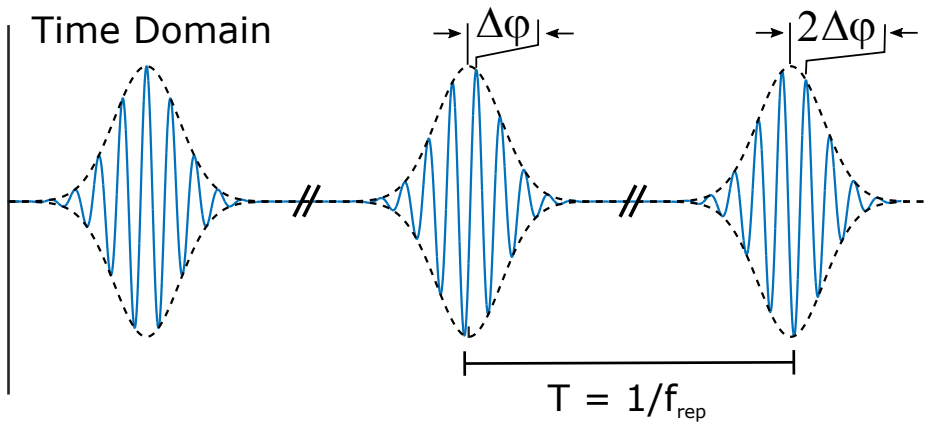

FIGURE 2.2. Time domain representation of a frequency comb. A modelocked laser emits a periodic train of ultrashort laser pulses in the time domain with period $T = 1/f_{\text{rep}}$ and pulse-to-pulse phase shift $\Delta\phi$, called the carrier-envelope offset.

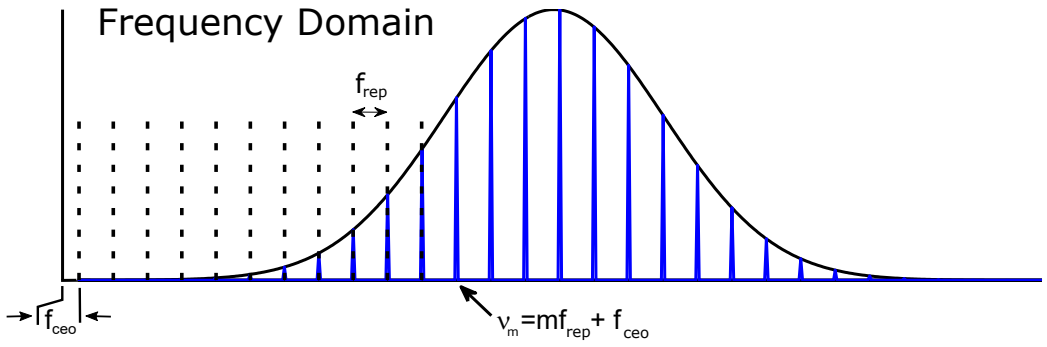

FIGURE 2.3. Frequency domain representation. The laser repetition rate leads to a "comb" of frequencies spaced at the repetition rate f_{rep}. The carrier-envelope phase shift leads to an offset from zero of $f_{\text{ceo}} = \frac{\Delta\phi}{2\pi T}$.

octave-spanning spectrum can either be obtained directly from the laser in certain cases [23], or by coupling some of the comb light into a highly nonlinear fiber to broaden the spectrum through supercontinuum generation [4, 22].

2.2 High Harmonic Generation

To reach VUV and XUV frequencies, a process called high harmonic generation (HHG) is commonly used to frequency upconvert near-IR light. HHG was first observed experimentally in the 1980s and is a nonlinear process that occurs when laser light is focused into a medium at intensities comparable to the medium's atomic binding potential to produce light at harmonics of the driving frequency [24, 25]. For the noble gases that are typically used, intensities on the order of 10^{13} W/cm^2 are required. It is also possible to generate attosecond pulses through the HHG process by controlling the phases of the generated harmonics [26].

2.2.1 Semi-Classical Model

At low intensities, an atom in a laser field can only undergo ionization if the photon energy $\hbar\omega$ is greater than ionization potential U_i of the atom. However, if the photon energy is too low, it is possible for multiple photons to be absorbed simultaneously to reach the ionization threshold. This process is called "multiphoton ionization" and is described in the perturbative regime. At higher intensities, "tunneling ionization" becomes the dominant mechanism which is characterized by the electron tunneling through the partially suppressed Coulomb barrier. To determine which ionization regime is relevant, the Keldysh parameter γ is used and is defined as

$$\gamma = \sqrt{\frac{U_i}{2U_p}}. \tag{2.2}$$

When $\gamma \gg 1$, the multiphoton regime applies and when $\gamma \ll 1$, tunneling ionization is the relevant mechanism. In this expression, U_i is the atomic ionization potential

and the ponderomotive energy U_p of the electron is given by

$$U_p = \frac{e^2 E^2}{4\omega^2 m_e} \tag{2.3}$$

where e is the electron charge, m_e the electron mass, E the laser electric field, and ω the laser frequency. An alternate way to think about γ is that it represents a ratio of the tunneling ionization time to the period of the laser's optical cycle [27].

In the strong field regime when $\gamma \ll 1$, an intuitive semi-classical model can be used to describe the HHG process. This is called the "three step model" and was originally developed by Kulander and Corkum in the early 1990s and is shown in Figure 2.4 [28, 29]. While a rigorous quantum mechanical model has been developed to describe HHG [30], this dissertation will focus only on the semi-classical approach as it captures all of the essential physics.

The first step in the model is ionization. In the absence of a strong laser field, an electron is bound to its parent atom in a Coulomb potential. When an intense laser field is applied to the atom, the potential is distorted and the electron can tunnel through the partially suppressed barrier (Step 1, Fig. 2.4).

Once the electron is freed into the continuum it is accelerated by the laser's electric field (Step 2, Fig. 2.4). Half of an optical cycle later, the electric field reverses sign and accelerates the electron back towards the parent atom. Depending on the phase of the driving field at the time of ionization, the electron wavepacket can follow different trajectories and return to the atom with different energies. For example, electrons that are ionized before the peak of the laser electric field will never return to the parent atom while electrons released at the peak return with zero energy and do not lead to harmonic generation.

If the electron trajectory leads to recollision with the atom, the energy acquired in the laser's electric field is emitted as a photon at harmonics of the fundamental frequency (Step 3, Fig. 2.4). The energy of the emitted photon is determined by the sum of the kinetic energy acquired after ionization and the atomic ionization potential

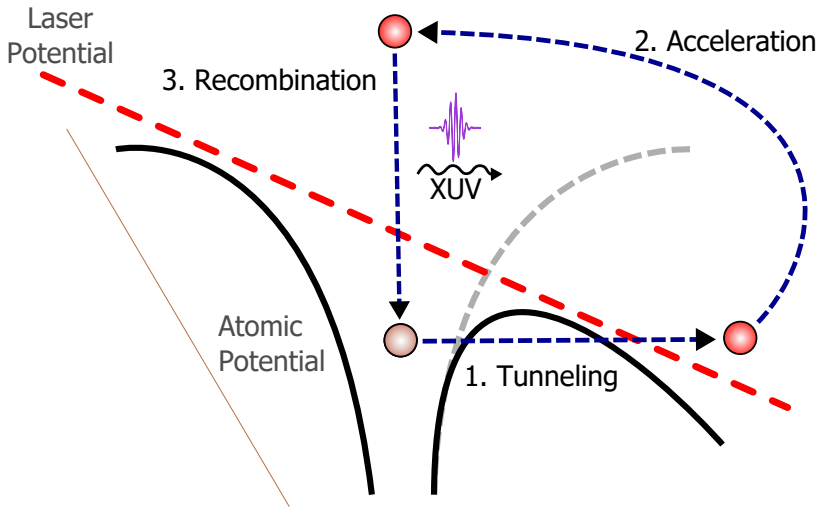

FIGURE 2.4. Three step model for high harmonic generation. 1) The laser's electric field distorts the atomic potential and the electron tunnels through the suppressed barrier. 2) The freed electron is accelerated by the electric field. 3) When the electric field reverses sign, the electron can re-collide with the parent atom releasing energy at harmonics of the fundamental frequency.

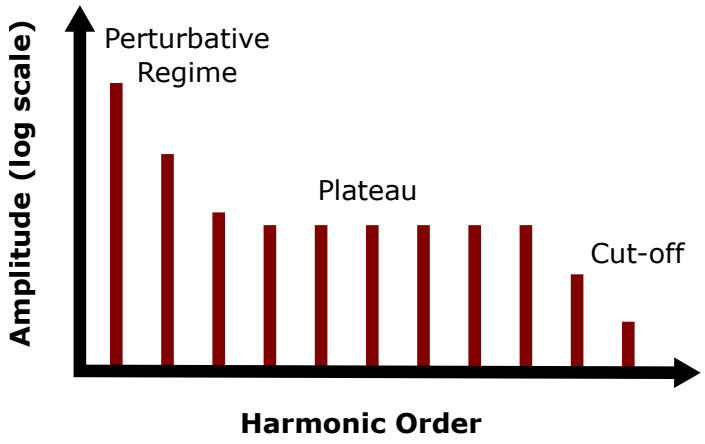

FIGURE 2.5. Typical spectrum obtained from high harmonic generation. Low-order harmonics in the perturbative regime exhibit a strong intensity decay with increasing order. The plateau region is characterized by approximately equal intensity harmonics up to the cut-off wavelength where the intensity quickly drops.

$\hbar\omega = E_{\text{kin}} + U_i$. The electron kinetic energy E_{kin} is a function of the phase of the driving field. According to the model, the maximum energy that can be acquired by the electron in the laser electric field is $3.17U_p$ and occurs at a driving field phase of 17°. This leads to a harmonic cutoff given by

$$\hbar\omega_{\text{cutoff}} = 3.17U_p + U_i. \tag{2.4}$$

Together, Equations 2.3 and 2.4 show that the cutoff energy can be increased by using a higher laser intensity or a longer wavelength for the driving field.

Because recollision events occur twice each cycle of the fundamental driving field ($T/2$), the spacing of harmonics in the frequency domain is $2\omega_0$. This leads to a frequency spectrum consisting of only odd-order harmonics starting with the fundamental frequency as shown in Figure 2.5.

2.2.2 Phase Matching

In macroscopic targets, efficient production of high harmonic radiation from the driving field is only achieved when certain "phase matching" conditions are met (i.e. the phase mismatch between the driving laser and the harmonics is minimized) [31, 32].

The phase mismatch $\Delta\phi$ is given by

$$\Delta\phi = q\phi_1 - \phi_q \tag{2.5}$$

where ϕ_q is the phase of the harmonic light of order q and ϕ_1 is the phase of the fundamental driving frequency. Perfect phase matching is met when $\Delta\phi = 0$.

For the fundamental field at frequency ω_1, the phase ϕ_1 of the field after propagating through the gas jet a distance z from the cavity focus is

$$\phi_1 = (1 + \Delta n_{\mathrm{gas}}(\omega_1) + \Delta n_{\mathrm{plas}}(\omega_1))kz - \tan^{-1}(\mathrm{z/z_R}) \tag{2.6}$$

where k is the vacuum wavenumber, Δn_{gas} is the change in refractive index due to the neutral gas density and Δn_{plas} the change due to the plasma. The last term, called the Gouy phase shift, is a geometrical effect due to the propagation of a Gaussian beam with Rayleigh range z_R through a focus. In terms of the beam waist w_0, the Rayleigh range is defined as $z_R = \pi w_0^2/\lambda$.

Similarly, it is possible to calculate the phase of the harmonic field of order q propagating through the same medium:

$$\phi_q = (1 + \Delta n_{\mathrm{gas}}(\omega_q) + \Delta n_{\mathrm{plas}}(\omega_q))k_q z - \tan^{-1}(\mathrm{z/z_{Rq}}) + \alpha_{\mathrm{q}}\mathrm{I(z)} \tag{2.7}$$

The addition of the final term compared to Eq. 2.6 arises from the fact the phase of the harmonic light depends linearly (with coefficient α_q) on the intensity at which it was created [32]. The intensity $I(z)$ for a Gaussian beam is

$$I(z) = \frac{I_0}{1 + (z/z_R)^2} \tag{2.8}$$

where I_0 is the intensity at the focus.

To obtain the total phase mismatch $\Delta\phi$, Eqs. 2.6 and 2.7 are subtracted. However, with the exception of the intensity-dependent atomic phase contribution, phase shifts on the fundamental are multiplied by the harmonic order as in Eq. 2.5 and will tend to dominate the phase shifts of the harmonics. If this is true, the phase mismatch can be simplified to

$$\Delta\phi \approx (\Delta n_{\mathrm{gas}}(\omega_1) + \Delta n_{\mathrm{plas}}(\omega_1))qkz - \tan^{-1}(\mathrm{z}/\mathrm{z_R}) + \alpha_{\mathrm{q}}\mathrm{I(z)}. \tag{2.9}$$

The Gouy phase shift and the atomic phase term have opposite signs and can often be made to cancel each other out [33]. In practice, this can be often be accomplished by fine tuning the position of the gas jet relative to the cavity focus.

When phase matching considerations are taken into account, the overall efficiency of the HHG process is typically no better than 10^{-6} in gas jets. If hollow core gas-filled fibers are used instead, efficiencies on the order of 10^{-5} can be achieved [33]. More complicated geometries involving quasi-phase matching have also been demonstrated but neither of these approaches can be used in the enhancement cavity approach described in the following chapter due to the high losses [34].

Chapter 3

Intracavity High Harmonic Generation

In order to reach peak intensities sufficient to ionize the target gas for HHG, the initial oscillator pulse train must be amplified. In many HHG experiments, this is accomplished using a multi-pass regenerative amplifier that amplifies a single pulse from the original pulse train and can operate at up to kHz-level repetition rates [35, 36, 37]. However, maintaining the full coherence of the frequency comb in this kind of direct amplification is not possible with the current state-of-the-art laser systems.

Alternatively, as laser technology improves, it may be possible to directly amplify the frequency comb and achieve peak pulse intensities high enough for HHG. To date, single pass HHG comb generation has been demonstrated at repetition rates up to 20.8 MHz but because of the tight focusing geometry required, phase matching was not achieved and the overall harmonic yield was very low [38].

To date, the most effective approach to creating frequency combs in the VUV and XUV was first demonstrated by Jones et. al. [39] and Gohle et. al. [40] in 2005 and utilizes a passive femtosecond enhancement cavity (fsEC) to effectively recycle the pulses emitted by a near-IR frequency comb. This technique is called "intracavity high harmonic generation" (IHHG) and these cavities can provide energy enhancements up to about 1000x, depending on the cavity configuration, and can enable peak intensities above 10^{14} W/cm^2. Since the initial demonstrations, power levels in the output coupled harmonics have increased from nW levels to the 100μW level and can cover wavelengths down to 12 nm [41, 42].

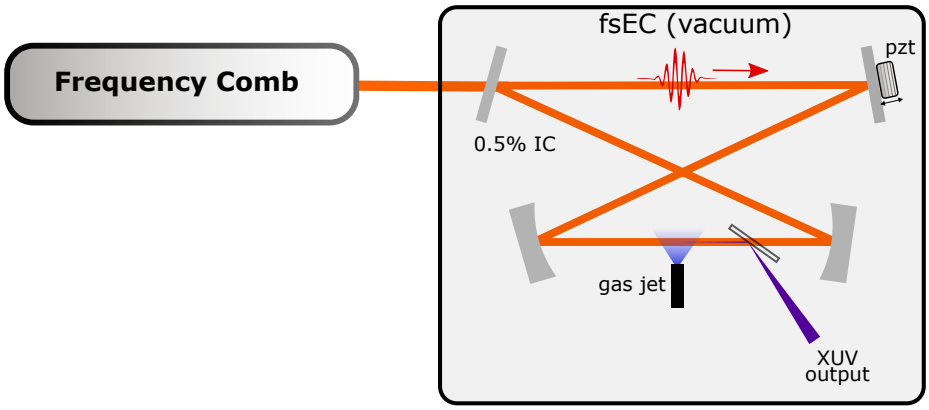

FIGURE 3.1. Schematic of fs enhancement cavity (fsEC). The fsEC passively amplifies the output pulse train of a frequency comb laser by recycling the pulse energy inside of the resonator. The amplification factor can be tuned by changing the input coupler (IC) percentage. Harmonics are coupled out of the cavity by a thin window placed at Brewster's angle for the circulating fundamental pulse.

3.1 Femtosecond Enhancement Cavity (fsEC)

3.1.1 Basic Principles

In their most common form, fsECs are arranged in a ring-cavity geometry and consist of a single partially reflective input coupler, two curved mirrors, and at least one flat mirror that is bonded to a piezo-electric transducer to compensate for mechanical and thermal fluctuations (see schematic in Figure 3.1).

Two key concepts are needed to describe the behavior of fsECs: free spectral range (FSR) and cavity finesse $\mathcal{F}$. The FSR is simply a measure of the frequency-domain resonance spacing and for a ring cavity in the absence of dispersion, it is given in terms of the speed of light c and the cavity length l as:

$$\text{FSR} = \frac{2\pi c}{l}. \tag{3.1}$$

The cavity finesse is a related quantity and is defined as the ratio of the FSR to the

FWHM cavity linewidth $\Delta\omega$:

$$\mathcal{F} = \frac{\text{FSR}}{\Delta\omega}. \tag{3.2}$$

Equivalently, if the cavity linewidth is expressed in terms of the total cavity losses and FSR, the finesse can be given solely in terms of the cavity loss percentage L, independent of the cavity length l. For the small values of L found in fsECs, this reduces to [43]:

$$\mathcal{F} \approx \frac{2\pi}{L}. \tag{3.3}$$

This relationship allows a straightforward estimation of the total intracavity losses by simply measuring the cavity linewidth or photon lifetime.

The maximum pulse energy enhancement factor $\mathcal{N}$ that can be supported by an fsEC with input coupling percentage T and total cavity loss percentage L is given by [43]

$$\mathcal{N} = \frac{P_{\text{circ}}}{P_{\text{inc}}} = \frac{4T}{L^2} \tag{3.4}$$

where P_{circ} and P_{inc} are the circulating and incident average powers respectively. The maximum enhancement occurs when the input coupling equals the additional round trip cavity losses – a condition known as *impedance matching*. A typical fsEC with a $T = 1\%$ input coupler will thus have an impedance-matched maximum enhancement of 400. Additional scattering losses in the cavity of 0.1% would reduce the maximum enhancement to about 330.

In addition to the power enhancement of the fsEC, it is important to determine the properties of the fundamental spatial mode. This is useful for mode-matching the incident beam to the cavity as well as calculating the focal spot size, peak intensity, and optimal HHG phase matching. For a rigorous treatment of Gaussian beams and optical resonators using the ABCD approach below, see Chapters 17 and 21 in [43].

In paraxial optics, a ray can be traced through an optical system consisting of lenses and curved mirrors by using a cascaded sequence of "ABCD matrices". In this approach a geometrical ray at distance r_0 from, and angle θ_0 relative to, the optical

axis is transformed by an optical system described by an ABCD matrix to yield a new ray given by r and θ:

$$\begin{pmatrix} r \\ \theta \end{pmatrix} = \begin{pmatrix} A & B \\ C & D \end{pmatrix} \begin{pmatrix} r_0 \\ \theta_0 \end{pmatrix}. \tag{3.5}$$

The individual matrix elements A, B, C and D are determined by multiplying the individual matrices describing each optical component in the system. For example, a lens (or other focusing element) with focal length f is described by the matrix A = 1, B = 0, C = -1/f, D = 1 and free space propagation of distance d is given by A = 1, B = d, C = 0, D = 1. Constructing the ABCD matrix for a system of n elements labeled in ascending order as seen by an optical ray would be done by calculating

$$\begin{pmatrix} A & B \\ C & D \end{pmatrix} = \begin{pmatrix} A_n & B_n \\ C_n & D_n \end{pmatrix} ... \begin{pmatrix} A_1 & B_1 \\ C_1 & D_1 \end{pmatrix}. \tag{3.6}$$

The fundamental mode of the fsEC is a Gaussian beam described by spot size $w(z)$ and the wavefront radius of curvature $R(z)$, which are both functions of the propagation distance z from the beam waist w_0. They are given by

$$w(z) = w_0\sqrt{(1 + z^2/z_R^2)} \tag{3.7}$$

$$R(z) = z + z_R^2/z \tag{3.8}$$

where is $z_R = \pi w_0^2/\lambda$ is called the Rayleigh range.

When discussing the propagating of Gaussian beams through an ABCD optical system, it is useful to use the "complex beam parameter" q which can be written in terms of $w(z)$, $R(z)$, and wavelength λ:

$$\frac{1}{q} = \frac{1}{R(z)} - i\frac{\lambda}{\pi w^2(z)}. \tag{3.9}$$

Since a stable resonantor mode must be identical after a round trip, the value of q should not change after passing through the ABCD system. In this case we must have

$$q_n = \frac{q_{n-1}A + B}{q_{n-1}C + D}. \tag{3.10}$$

By setting q_{n-1} equal to q_n and solving for q_n, the beam parameter of the Gaussian beam in the cavity is determined to be

$$\frac{1}{q} = \frac{D-A}{2B} - \frac{i}{2B}\sqrt{4-(A+D)^2} \tag{3.11}$$

and thus by inspection with Equation 3.9 the spot size and radius of curvature can be obtained.

3.1.2 Output-Coupling the Harmonics

To couple the harmonic light out of the cavity a variety of output coupling methods have been proposed. The simple approach taken in the initial IHHG experiments, and the one used in this dissertation, was to place a thin sapphire window just after the gas jet [39, 40]. The window is placed such that it is at Brewster's angle for the fundamental frequency and thus adds almost zero loss to the fundamental beam. However, because the refractive index of sapphire is very different at VUV/XUV wavelengths, these wavelengths reflect off of the plate at about 10% efficiency [39, 40]. The Brewster plate is often made of high-purity sapphire or fused silica due to the thermal properties and high damage threshold of these materials. Furthermore, it is crucial to have the highest possible surface quality to avoid introducing losses to the fundamental cavity mode and reducing the achievable pulse enhancement.

Figure 3.2 shows the focal region of the fsEC while generating harmonics. The blue region in the center is the plasma formed in the gas jet and the circular sapphire plate to the right is the harmonic output coupler. The plate must be placed close enough to the focus to avoid clipping the beam reflected off the curved mirror behind it but not so close that the smaller beam size near the focus induces damage or nonlinear effects. It is also important to note that the thickness of the window should be kept as small as possible to reduce the amount of dispersion (see Section 3.1.4) but not so small that surface quality and thermal effects become significant. Typical thicknesses range from 100 μm to 500 μm.

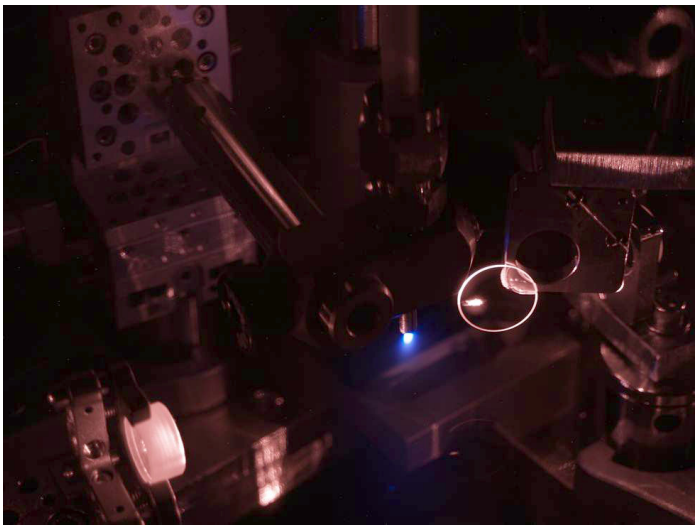

FIGURE 3.2. Focal region of the fsEC showing plasma formation at the output end of the gas jet. To the right of the gas jet is the circular sapphire output coupler for the harmonics.

Alternative output coupling methods that have been demonstrated or proposed include a high reflector with a grating etched onto the surface [44, 45], a holed mirror that transmits on-axis harmonics with limited losses to the fundamental cavity mode [46, 47, 48], non-collinear output coupling using two crossed fundamental beams [49, 50], a grazing incidence coated plate [51], and a wedge-on-mirror coupler [52].

3.1.3 Cavity Stabilization

In order to achieve good enhancement of the incident pulse train, both the repetition rate and offset frequency of the incident laser must be matched to the fsEC. In practice this requires compensating for mechanical and thermal fluctuations of the cavity length, intracavity dispersion, or changes in air density outside of the cavity. This is accomplished using an active-feedback stabilization loop (also known as a servo loop) containing a feedback actuator in the cavity itself, in the laser, or in the beam path between the laser and fsEC. In many cases, the laser is more stable and has

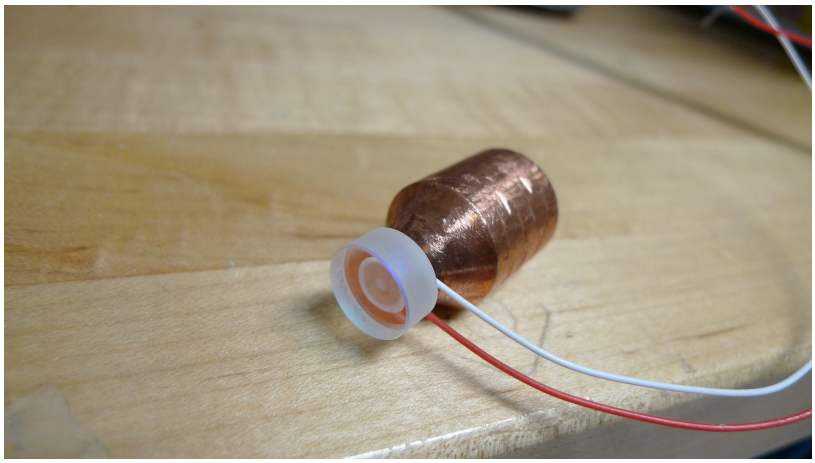

FIGURE 3.3. Typical mirror/PZT assembly used for cavity stabilization. The mounting block is made of copper to dampen the intrinsic mechanical resonances of the assembly. The individual elements are bonded together with Torr Seal for vacuum compatibility.

better noise properties than the fsEC and so it is advantageous to place the feedback actuator in the fsEC. This is commonly done by gluing one of the fsEC mirrors to a small ceramic piezo-electric transducer (PZT) that provides small corrections to the cavity length. Figure 3.3 shows a typical mirror/PZT assembly for use in the fsEC. The copper mounting block is based off of the design in [53] and serves to dampen the strongest mechanical resonances of the mirror/PZT combination. With this design we were able to achieve servo locking bandwidths up to 100 kHz, thus suppressing nearly all acoustic noise and providing a robust lock. For short term operation of the fsEC, it is often not necessary to actively stabilize f_{ceo}, especially if the source laser is sufficiently quiet. Instead, f_{ceo} can be manually tuned to match the cavity offset frequency and still achieve good enhancement.

In addition to the actuator that provides the correction, the stabilization loop must have an error signal that shows the deviation of the laser from some reference. The key feature of the error signal is that it must be bipolar. In other words, its value

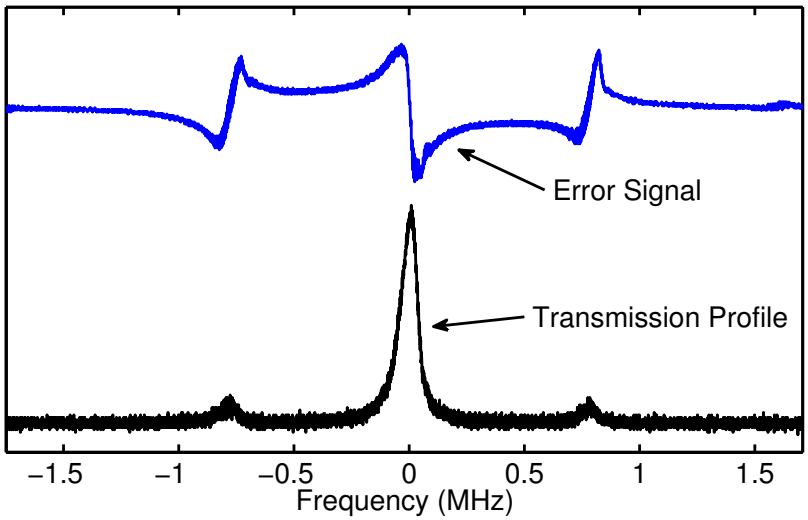

FIGURE 3.4. Typical error signal (blue) for stabilizing an enhancement cavity to a frequency comb. The black curve shows the intracavity power as the cavity length is scanned through resonance with modulation sidebands at 800 kHz for generating the error signal. The peak of the resonance corresponds to the central zero-crossing of the error signal.

should be zero if the laser is exactly on resonance with the cavity and change sign as it passes through this resonance.

Obtaining this error signal is most commonly done with the optical Pound-Drever-Hall (PDH) technique [54] originally developed for stabilizing cw lasers to optical cavities but equally applicable for fs lasers [55]. To get the PDH error signal, an RF modulation is applied to the incident laser by passing the beam through an electro-optic modulator or by dithering a PZT. If the modulation frequency is sufficiently larger than the cavity line width, sidebands are created that provide a phase-sensitive reference. A heterodyne beat signal between the reflected and intracavity light can be recorded on a photodiode and demodulated against the RF source to produce the desired bipolar error signal with zero value on-resonance (see Figure 3.4).

The third part of the stabilization loop is made up of the electronics that control

the locking and determine the loop's transfer function (i.e. frequency response). A combination of homemade and commercial servo loop filters were used for the locks in this dissertation though all operate on the same principles. These filters provide proportional gain and up to two stages of integral gain at low frequencies. If high bandwidth actuators like electro-optic modulators (EOMs) or acousto-optic modulators (AOMs) are used, it is often beneficial to use a servo that includes derivative gain at high frequencies in order to flatten out the phase response and achieve bandwidths beyond the 100 kHz level. The servo frequency corners that determine the loop response and the overall gain are adjusted manually to achieve the best performance for each individual lock.

3.1.4 fsEC Dispersion Control

When designing an enhancement cavity for use with femtosecond pulses, it is critical to account for the effects of group velocity dispersion (GVD). GVD is defined as the derivative of the inverse of the group velocity v_g with respect to the angular frequency ω:

$$\text{GVD} = \frac{\partial}{\partial \omega} \frac{1}{v_g}. \tag{3.12}$$

In other words, GVD changes the spectral phase as a function of frequency for a pulse propagating through a dispersive medium or when encountering a dispersive element. GVD can also be expressed as the group delay dispersion (GDD) per unit length. Since mirrors have no "length", their dispersion properties are typically expressed in terms of GDD at a given wavelength. Dielectric mirrors like those used in fsECs typically have a GDD curve like the one shown in Figure 3.6 which has a zero-crossing at the center wavelength of the dielectric coating. Mirrors with different center wavelengths can be combined to tune the cavity GDD properties for optimal enhancement of the incident laser spectrum.

Figure 3.5 shows how mirror dispersion leads to a change in the spacing of the

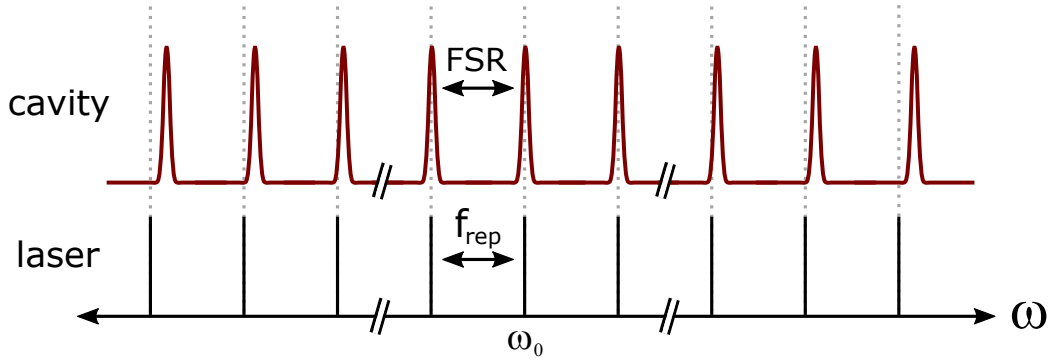

FIGURE 3.5. Aligment of evenly-spaced frequency comb modes (black lines) to enhancement cavity modes (red lines) showing the effects of dispersion. Near the center frequency ω_0, the cavity and comb modes have an identical spacing given by FSR $= f_{\text{rep}}$. However, mirror dispersion changes the cavity mode spacing away from ω_0 leading to a finite optical bandwidth that can be coupled to the fsEC.

cavity modes and limits the optical bandwidth that can be coupled to an fsEC. The width of the cavity modes is determined by the finesse and thus by using a larger input coupler, a broader range of comb frequencies can be coupled efficiently to the fsEC, though at the cost of reduced buildup.

To see how dispersion affects the pulse, consider the spectral phase $\Phi(\omega)$ expanded about the center frequency ω_0 and with dispersion coefficients Φ_n:

$$\Phi(\omega) = \Phi_0(\omega) + \Phi_1(\omega - \omega_0) + \Phi_2(\omega - \omega_0)^2/2 + \Phi_3(\omega - \omega_0)^3/6 + ... \tag{3.13}$$

When the pulse train is optimally matched to the fsEC, Φ_0 and Φ_1 are set to 0 as these affect only the round trip carrier phase and group delay. However, the parameters Φ_2 and Φ_3 are the second and third order dispersion coefficients respectively and can affect the pulse duration. Higher order terms exist but their affect on pulses around 100 fs is usually not significant.

Coupling a broad spectrum of frequencies efficiently to an fsEC requires that the cavity modes align well to the modes of the incident laser. However, because of

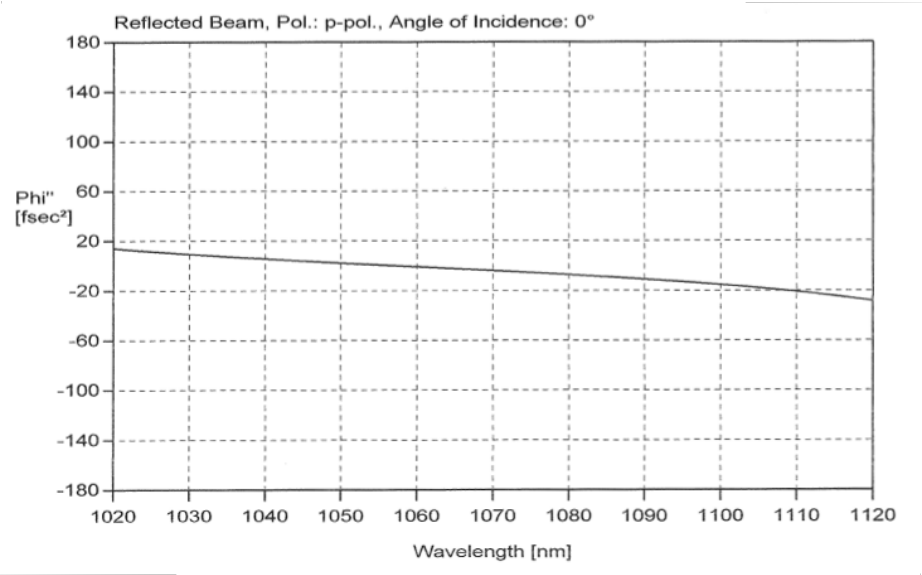

FIGURE 3.6. GDD curve for a Layertec 100324 enhancement cavity mirror.

dispersion from the dielectric mirror coatings, the fsEC modes are not evenly spaced over the full bandwidth of the comb spectrum and only a finite spectral bandwidth can be coupled to the cavity. Thus, finding the right combination of mirror coatings to tune the cavity group delay dispersion (GDD) is very important to achieving a high enhancement factor.

To facilitate this GDD tuning, a software program called GVDCalculator was written in MATLAB to simulate the expected energy enhancement, intracavity spectrum, and transform-limited pulse duration for various mirror coatings and dispersive elements. A screenshot of the program showing its capabilities is shown in Figure 3.7. Mirror dispersion curves for a variety of coatings used in the fsEC were obtained from the mirror manufacturer (Layertec) and imported. The program also includes dispersion parameters for a variety of materials and gases and allows for the addition of new ones. The estimated GDD plot in Figure 3.7 shows that the ability to couple a very broad spectrum into the cavity is currently limited by mirror dispersion (indicated by the significant slope of the mirror GDD line). If shorter pulses are desired, custom

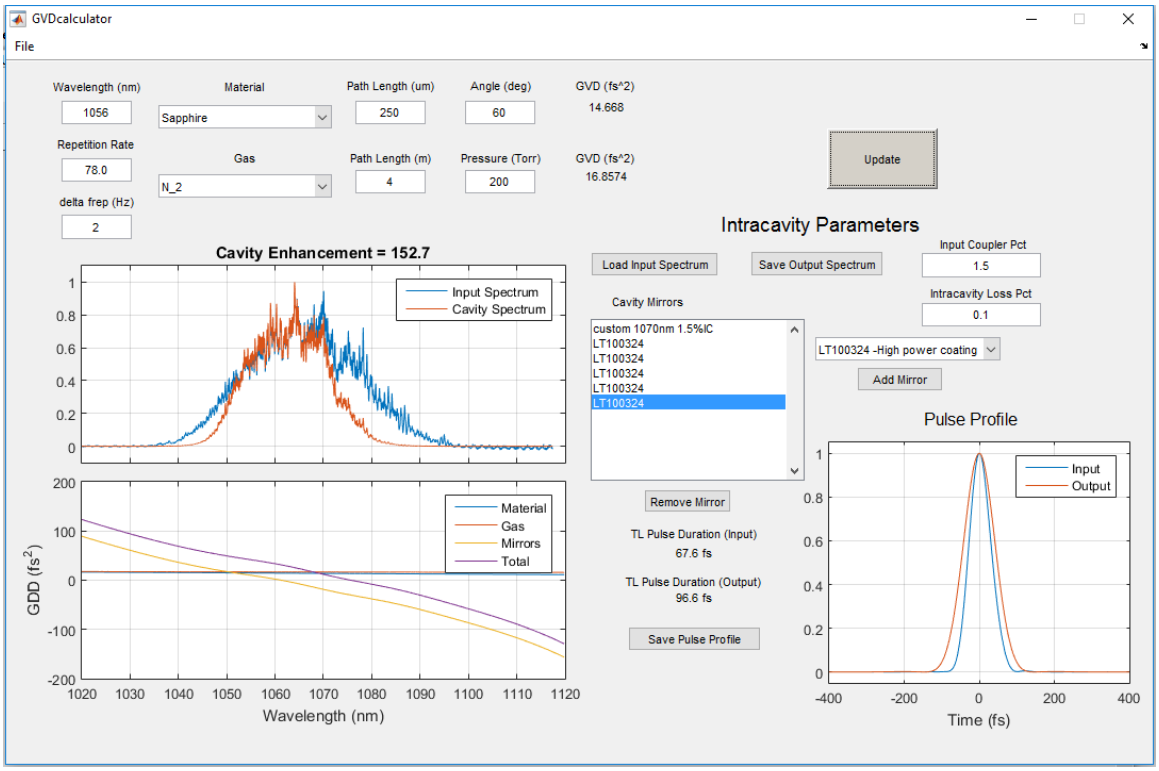

FIGURE 3.7. Screenshot of fsEC dispersion simulation software. The program allows the user to import an existing laser spectrum and determine how well it can couple to an enhancement cavity with the specified mirror coatings, input coupler, and material dispersion. The incident laser spectrum can be optimized by adjusting both the center "locking" frequency and the detuning of the mode spacing.

mirror coatings are required [56].

For wavelengths near 1 μm, dispersion due to the thin sapphire Brewster window has only a small effect on the intracavity spectrum though it can be used to fine-tune the zero-GDD point of the cavity. The spectrum can be more readily tuned by adjusting the alignment of the incident laser modes. Figure 3.8 shows a comparison of experimental and simulated spectra for a few different values of comb detuning. The experimental curves are obtained with an fsEC having a 1.5% input coupler, LT100324 mirror coatings for the remaining five mirrors, and a 250 μm sapphire plate. For this data, the comb is locked to a cw laser at 1070 nm and the repetition rate adjusted to manually align the comb modes to the cavity. The experimental incident spectrum is used as the input for the GVDCalculator simulation. As the detuning Δ between comb and cavity is increased, the spectrum is narrowed and the enhancement drops from just under 200 for $\Delta = 0$ Hz to about 80 for $\Delta = 6$ Hz.

3.1.5 fsEC Damage Limitations

One of the challenges with operating fsECs for HHG experiments is that intracavity power levels can limit the system performance by causing damage to cavity optics after extended operation. Damage can occur primarily by two different mechanisms: high peak power of the pulses in the fundamental beam or directly from the high energy harmonics. As an example, Figure 3.9 shows an fsEC curved mirror with damage to the dielectric coating after long-term irradiation by the combined IR and harmonic beams.

In work done in 2010 by Pupeza et al., it was demonstrated that damage due to the circulating fundamental field is primarily caused by high peak power on the mirror surfaces [57]. They found that the cavity was capable of supporting average powers of 72 kW with 2 ps pulses but when the pulse duration is reduced below 1 ps, the damage threshold rapidly drops to multi-kW levels. In order to achieve higher

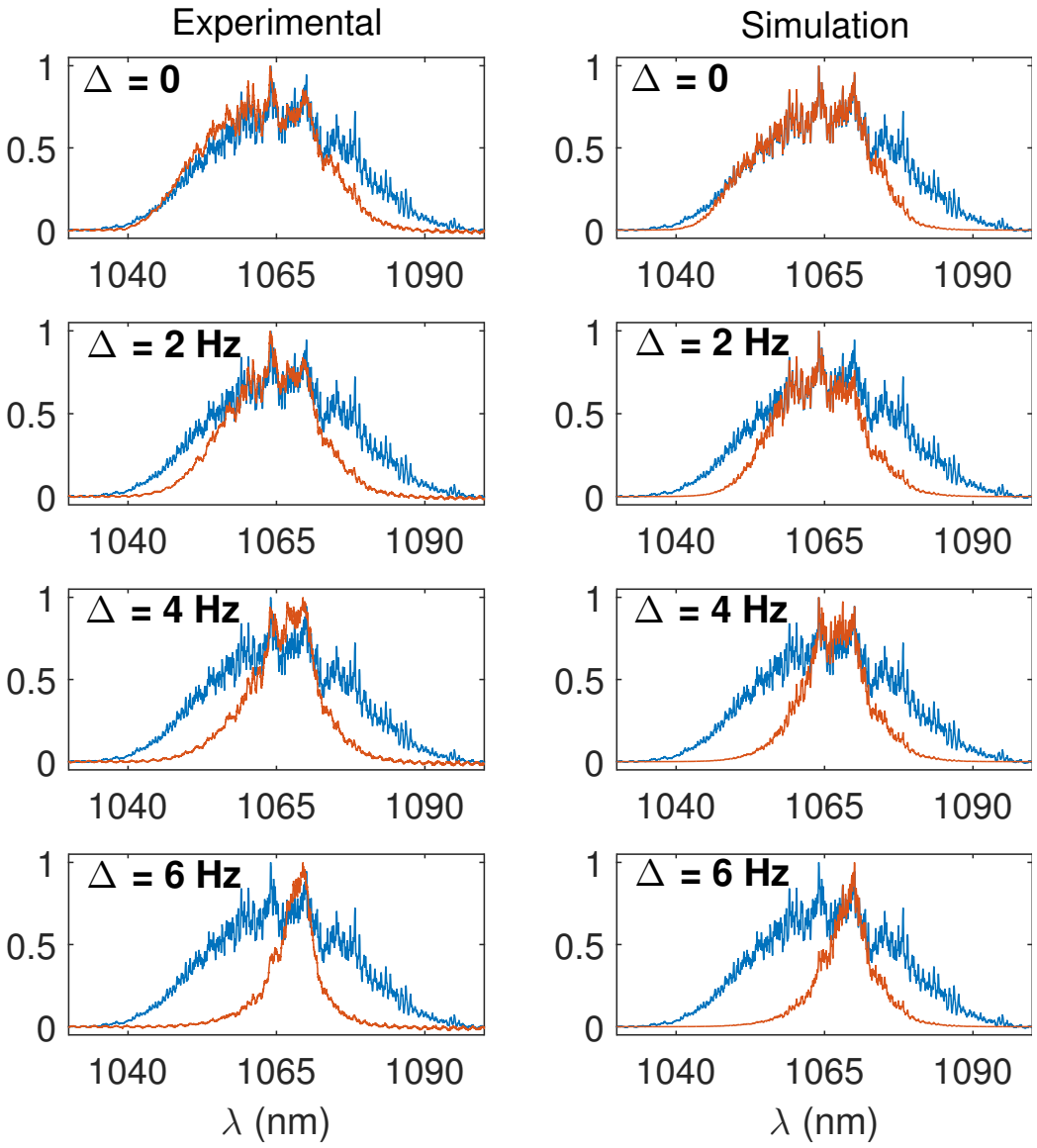

FIGURE 3.8. Comparison of experimental fsEC spectra (left column) with spectra obtained from the GVDCalculator simulations (right column) using the experimental laser spectrum as input at a few different values of the comb detuning. In the experiment the laser is locked at 1070 nm to a cw laser and the mode spacing is adjusted by changing the repetition rate. The blue curve on each plot shows the incident laser spectrum.

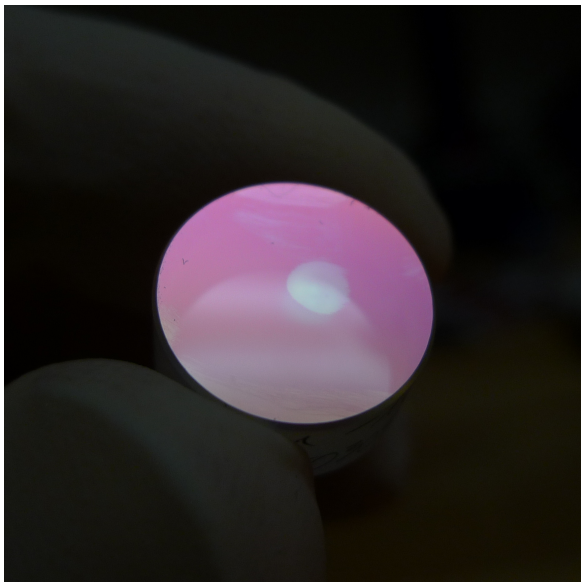

FIGURE 3.9. fsEC curved mirror showing visible damage region after irradiation with combined intense IR and XUV light.

intracavity powers, they concluded that advances in mirror coatings were required or changes to the cavity design be made that reduce the spot size at the mirrors.

Performance degradation in the fsEC due to the relatively high XUV photon flux is another possible source of damage [58, 59]. Physically, this effect arises due to contaminant hydrocarbons in the vacuum chamber interacting with the high energy photons. As a result, a layer of hydrocarbons builds up on the mirror surface causing a reduction in reflectivity and consequently the intracavity power. Figure 3.10 shows the Brewster plate output coupler under intense XUV irradiation. The harmonic beam path is visible because the chamber is backfilled with a small amount of oxygen which is subsequently ionized. The termination of the visible plasma line between the gas jet and window indicates that the window is absorbing the bulk of the high energy harmonics. Fortunately, a number of groups have reported that problems related to harmonic damage can be largely mitigated by introducing ozone (O_3) directly into the vacuum chamber [59, 60]. Ozone has a high oxidation potential and can serve to

etch away the contaminant layer or even prevent it from forming in the first place.

An additional approach to minimizing intracavity damage involves optimizing the cavity geometry to give larger spot sizes on the mirrors [61]. This can be accomplished for example by decreasing the radius of curvature of the two cavity curved mirrors. This has the effect of creating a small focal spot and thus, higher peak intensities, however there is a trade-off in phase matching that must be considered due to the increased Gouy phase shift in a tight-focusing geometry. There is also the possibility of using alternative cavity designs, such as an all-curved-mirror resonator as described in [61] or a cavity containing mirrors with negative curvature. This is an area that may benefit from further study as damage becomes increasingly problematic as the laser power continues to scale up.

3.2 Ti:Sapphire Results

Initial IHHG results from our group were based on a Ti:sapphire laser operating at 50 MHz repetition rate. The laser system and results are described in detail in [41]. Ti:sapphire lasers can provide a broad wavelength tuning range and their shorter wavelength compared to other fiber-based laser systems can improve the efficiency of HHG conversion. While it is challenging to amplify Ti:sapphire systems to average power levels achievable with fiber amplifiers, by utilizing a lower repetition rate, the achievable pulse energy can by just as high or even higher than systems operating beyond 100 MHz. To this effect, our group previously demonstrated a 7 W average power comb at 50 MHz repetition rate by actively injection locking a femtosecond amplification cavity (fsAC) [62]. Our first IHHG results used this system to seed an fsEC at 6 W average power to provide an incident pulse energy of over 100 nJ in 80 fs pulses. A schematic of the system is shown in Figure 3.11.

Depending on the input coupler used in the fsEC, the pulse energy could by enhanced up to 200 times to reach intensities up to 10^{14} W/cm^2. For the results

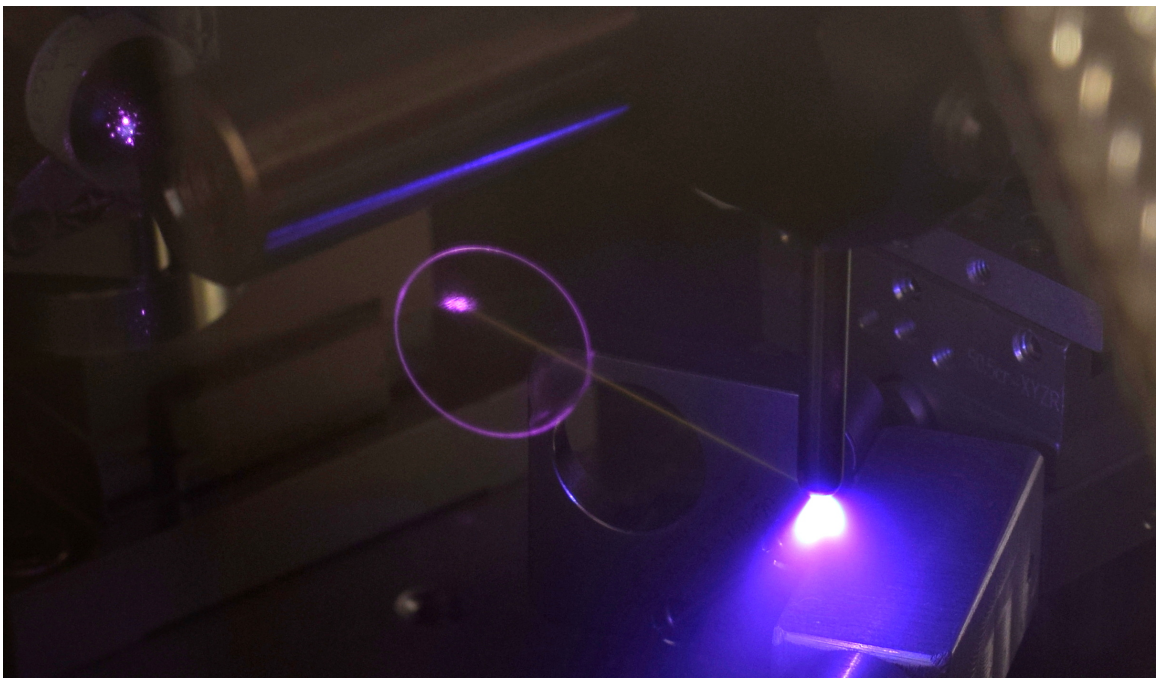

FIGURE 3.10. Focal region of the fsEC while in use showing the gas jet with strong plasma, sapphire plate output coupler, and one cavity curved mirror. The chamber was filled with about 1 mTorr of O_3 when this picture was taken. The harmonic beam path is visible between the gas jet and the sapphire plate due to direct ionization of the ozone by the high energy photons.

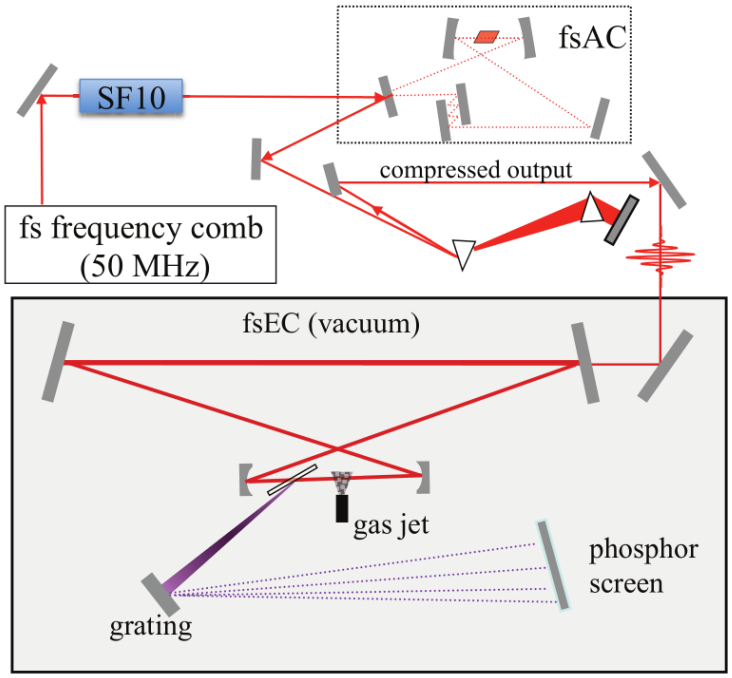

FIGURE 3.11. Schematic of the Ti:Sapphire-based IHHG system. A fs amplification cavity (fsAC) is used to amplify the 50 MHz pulse train up to 7 W average power while maintaining the full repetition rate of master oscillator. The pulses are compressed with a prism pair before seeding the fsEC.

shown in Figures 3.12 and 3.13, the fsEC used a 1% input coupler and 15 cm radius-of-curvature mirrors to achieve a beam size of $w_0 = 15\mu$m. The larger input coupling compared to previous IHHG demonstrations served to limit spectral filtering due to mirror dispersion and also to reduce the nonlinear effects associated with strong ionization. Furthermore, the increased mirror curvature compared to previous work reduced the Guoy phase mismatch described in Section 2.2.2, leading to increased overall harmonic production despite a lower peak intensity.

The out-coupled harmonics were reflected off of a concave Pt-coated grating and imaged onto a sodium salycilate phosphor screen. The resulting harmonic spectrum and grating efficiency is shown in Figure 3.12a for a backing pressure of 500 Torr and gas jet width of 300 μm. Figure 3.12b shows the 7th to 15th harmonics individually resolved on the phosphor screen and imaged onto a CCD camera.

The total power was measured after the grating with a NIST-calibrated photodiode positioned at the 11th harmonic with adjacent harmonic orders blocked. A maximum of 77 μW of output-coupled power recorded – at the time a record power for an XUV frequency comb – and demonstrated the potential of the IHHG approach as a bright source of coherent radiation in the VUV and XUV.

A plot of the total power at the 11th harmonic as a function of xenon backing pressure is shown in Figure 3.13 when a 100 μm gas jet is used instead of the 300 μm jet. While this jet orientation does not provide the best phase matching, the shorter interaction region allowed for more consistent operation of the fsEC because damage-related problems were less frequent. A clear saturation effect was observed at higher backing pressures and was attributed primarily to the reduction of intracavity pulse energy. This effect arises as the circulating cavity pulse acquires a nonlinear chirp due to ionization of the target gas and is addressed in detail in Chapter 4.

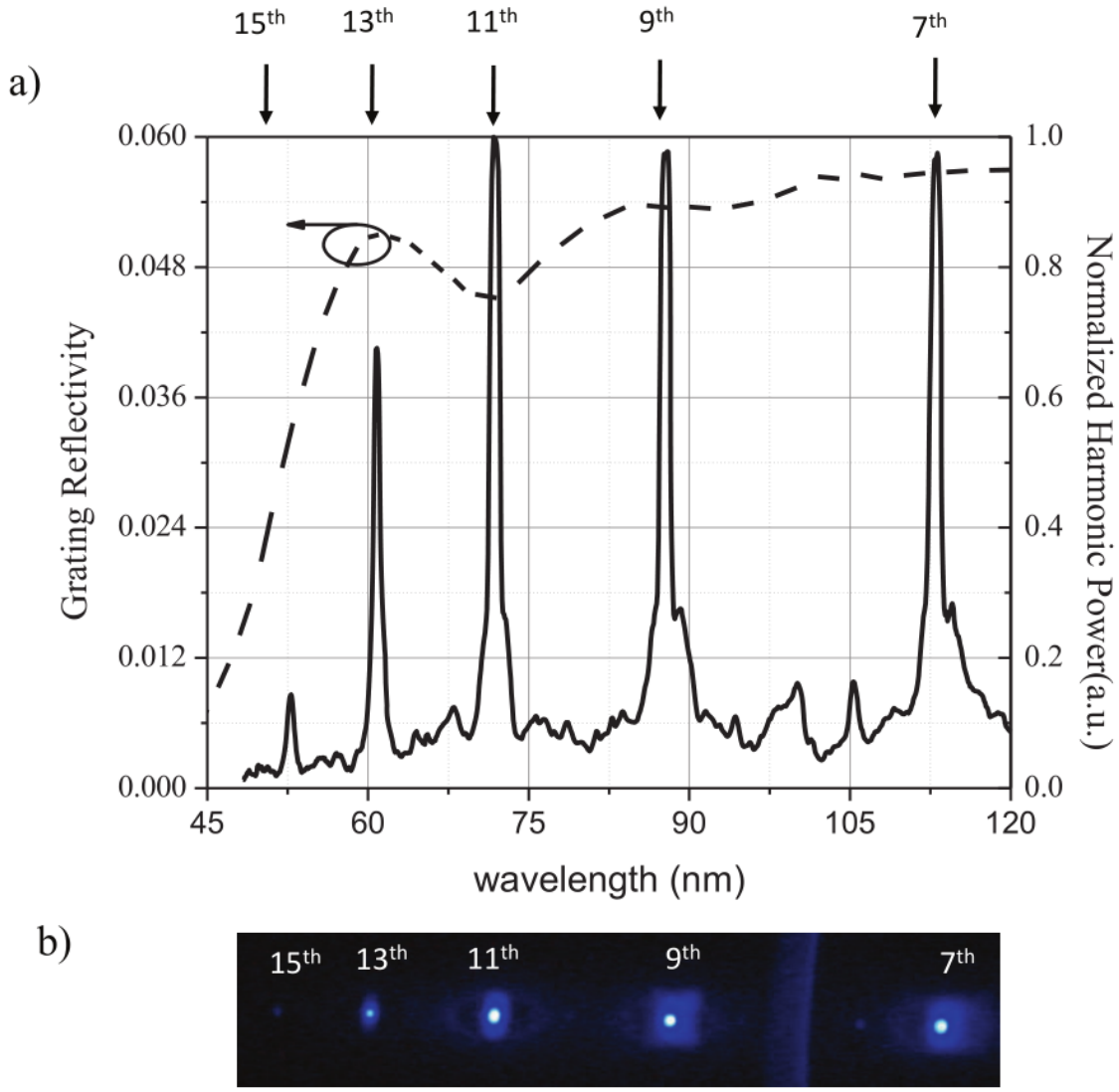

FIGURE 3.12. a) High harmonic spectrum obtained from fsEC seeded with a high power Ti:Sapphire frequency and theoretical diffraction grating efficiency. b) CCD image of resolved harmonic orders on a phosphor screen.

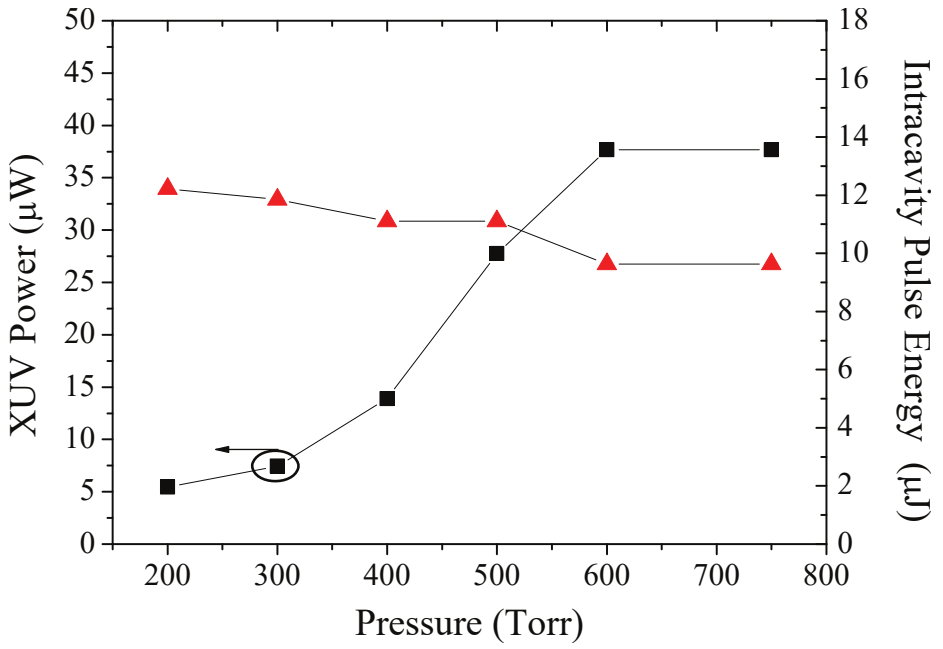

FIGURE 3.13. Measured power of the 11th harmonic (72 nm) and the corresponding intracavity pulse energy as a function of xenon backing pressure.

3.3 Yb Fiber Laser System

Though the results presented in [41] were promising, the system would not reliably run for periods of time exceeding a few minutes. Mirror damage, both due to the high intracavity powers and the presence of XUV radiation, would lead to degradations in the intracavity buildup over time. However, it has been reported that operating the fsEC at longer wavelengths seems to reduce the effects of damage [63, 41, 21].

Recent advances in fiber laser technology have allowed very high average power amplifier systems to be used with femtosecond pulsed lasers at drastically reduced cost compared to Ti:Sapphire systems. In the interest of pursuing dual comb spectroscopy (see Chapter 5), we decided to shelve the Ti:Sapphire laser and replace it with two identical ytterbium (Yb) fiber laser systems. In addition to cost savings and higher average powers, the day-to-day reliability of fiber-based lasers is improved over often temperamental Ti:Sapphire lasers and the longer operating wavelength (λ = 1064

nm) is believed to reduce intracavity fsEC damage.

3.3.1 Laser Oscillator

The primary frequency comb for each of the two systems is a homemade Yb fiber laser whose layout is shown in Figure 3.14. The laser contains a 65 cm section of Yb-doped gain fiber and a free space section containing a high efficiency grating pair (LightSmyth Technologies LSFSG-1000-3212-HP) for dispersion compensation and pulse optimization. A quarter and half waveplate are used in combination with a polarizer to initiate modelocking via nonlinear polarization evolution [64, 65]. The oscillator has a repetition rate of 78 MHz and the output is a collimated free-space beam with sub-100 fs pulses after compression with an additional external grating pair. The average power before the grating compressor is about 70 mW at 300 mW pump power. Figure 3.15 shows a typical laser spectrum with a center wavelength near 1060 nm – a value chosen to coincide with the zero-GDD crossing of the fsEC mirrors.

The laser contains a variety of different actuators that can be used for stabilization. An EOM provides high bandwidth modulation of the cavity length but has a limited amplitude range. To compensate for the larger fluctuations, a fast PZT/mirror combination can be used or the pump current can be modulated. An additional horizontally tiltable PZT-mounted mirror is located behind the grating pair to provide tuning of the offset frequency.

3.3.2 Power Amplifier

In order to produce sufficient power to seed the power amplifier (at least 500 mW), an initial "pre-amplifier" stage is added after the oscillator output. By leaving the external compression gratings between the oscillator and the pre-amplifier input, a nonlinear parabolic amplification scheme can be used to provide third-order disper-

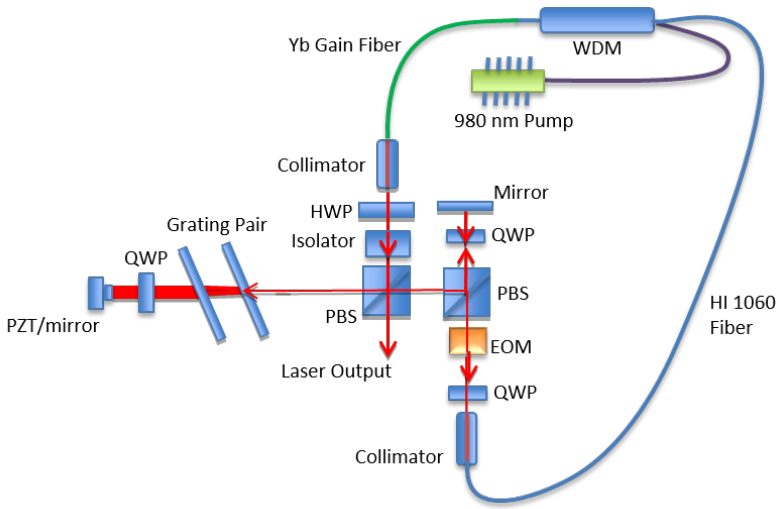

FIGURE 3.14. Yb fiber oscillator schematic. A free-space section (red beam path) allows inclusion of a grating pair for dispersion compensation and both an electro-optic modulator (EOM) and a mirror-mounted fast pzt for feedback stabilization. A quarter-wave plate (QWP) and a half-wave plate (HWP) placed near the fiber collimators are used to initiate modelocking based on nonlinear polarization evolution. The oscillator lasers produce sub-100 fs pulses at an average power of 70 mW. WDM: wavelength division multiplexer, PBS: polarization beam splitter.

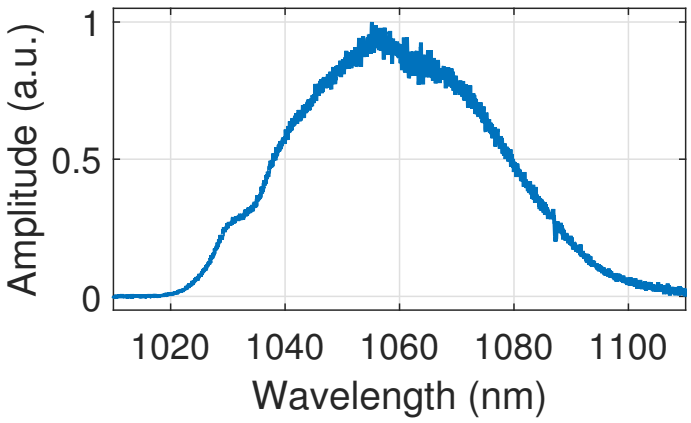

FIGURE 3.15. Typical optical spectrum of Yb laser oscillator.

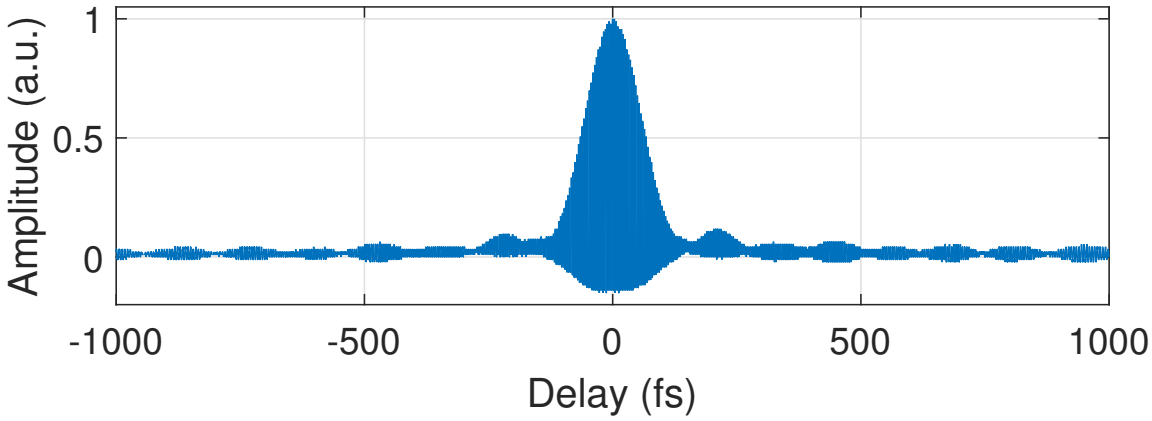

FIGURE 3.16. Measured interferometric autocorrelation of the 89 fs pulses emitted by the high power Yb fiber system. The small bumps in the wings of the pulse are caused by uncompensated third-order dispersion in the nonlinear amplifier.

sion compensation and ultimately provide better pulse compressibility after the final amplification stage [66, 67]. The grating separation is manually tuned to produce the shortest pulses after the final amplification stage by monitoring an interferometric autocorrelation trace of the high power pulses (see Figure 3.16). The pre-amplifier uses 5 m of double-clad Yb fiber (Nufern PM-YDF-5/130-VIII) and is pumped by up to 8 W of power at 980 nm. This amplification stage outputs 3 ps chirped pulses and brings the average output power to 2 W which is sufficient for seeding the PCF fiber.

The final amplification stage uses an OEM amplifier module (NKT Photonics aeroGAIN-BASE-1.1) consisting of a 3 m segment of photonic crystal fiber (PCF) that is pumped at 915 nm by a 120 W pump diode (NLight Pearl). The output end of the fiber is watercooled to prevent damage and reduce thermal beam-pointing instabilities. The PCF amplifier has a 31 μm mode field diameter, a polarization extinction ratio of $>$ 15 dB, and can support output powers up to 75 W. In our system, the amplifier is typically run at 80 W pump power and, after compression, produces 46 W average power and 89 fs FWHM pulses. A schematic of the complete amplifier chain is shown in Figure 3.17.

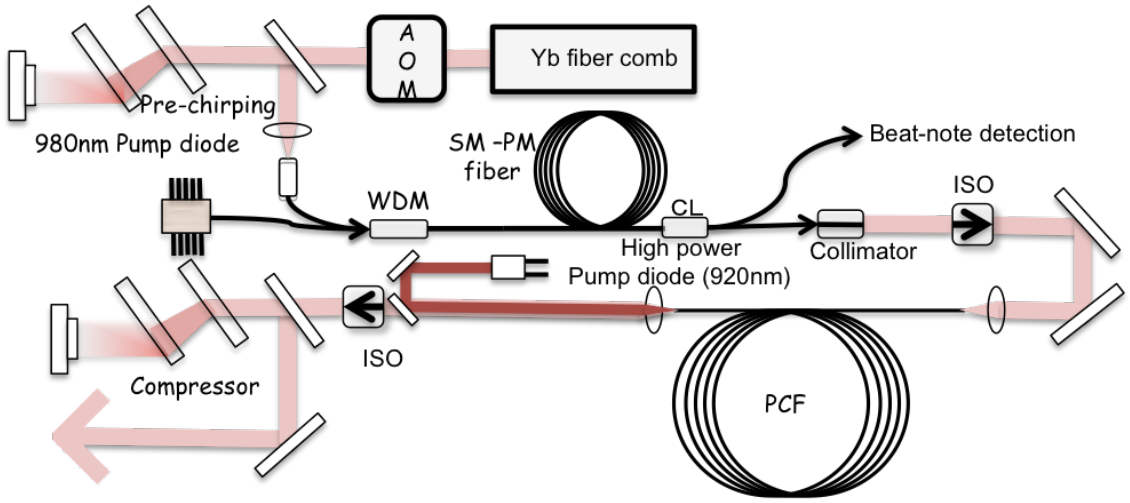

FIGURE 3.17. Schematic of the high power amplifier chain. A "pre-chirp" grating pair controls the pulse duration and chirp of the oscillator pulse train before seeding the nonlinear pre-amplifier. The 2 W output of the pre-amplifier is used to seed the 3 m long photonic crystal fiber (PCF) amplifier. After a final compression grating pair, the system emits 80 fs pulses at 50 W average power. WDM: wavelength division multiplexer, ISO: isolator, SM-PM fiber: single-mode and polarization maintaining fiber, CL: fiber coupler, AOM: acousto-optic modulator.

In order to protect the PCF amplifier from damage in the event that the laser loses modelock or the seed light gets blocked, a custom interlock circuit is used to quickly shut off the pump laser. By detecting the laser repetition rate before and after the amplifier and mixing them together, a dc signal is generated that is used to trigger a relay and switch the laser off before damage occurs.

Chapter 4

Intracavity Ionization

4.1 Experimental Challenges

One of the difficulties of operating an fsEC for HHG is that the highly nonlinear process of ionizing the target gas can induce significant phase shifts on the circulating intracavity pulse. In practical terms, this leads to instabilities in the stabilization if the feedback loop cannot adequately follow these resonance shifts. Prior to this work, the effects of the intracavity ionization were not well understood though it was evident that it was problematic under certain circumstances. For example, Figure 4.1 shows how strong ionization leads to locking instabilities. In the figure, the blue curve represents the intracavity power for a weak probe beam as a function of time and is initially very stable. When the plasma formation (green curve) is "turned on" by unblocking the high power frequency comb with a chopper wheel, the intracavity power immediately develops strong oscillations. However, the probe buildup quickly reverts to the desired behavior when the chopper wheel blocks the pump beam and plasma is no longer present in the cavity. In order to understand this effect and find ways to mitigate it, numerical simulations of the fsEC were created and an experimental technique developed to directly measure the plasma *in situ*.

4.2 Intracavity Plasma Simulations

A numerical model was developed to understand in detail how the intracavity ionization affects the dynamics of the circulating intracavity pulse. This enables a prediction

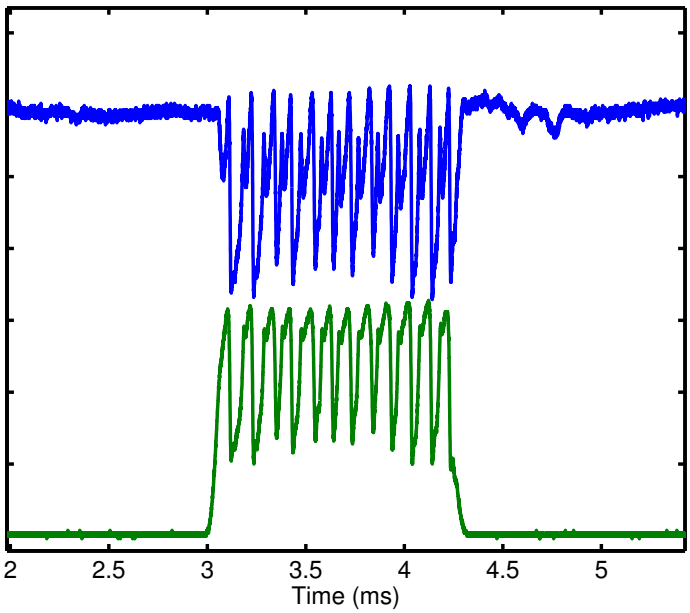

FIGURE 4.1. Large oscillations in fsEC intracavity power (blue curve) when strong intracavity ionization (green curve) is present.

of the intracavity ionization densities and the threshold at which active stabilization to the cavity resonance becomes complicated by the nonlinear response of the cavity.

4.2.1 One Dimensional Spatial Model

The evolution of the intracavity pulse is calculated by solving the Nonlinear Schrödinger Equation (NLSE) in one spatial dimension plus time as it propagates through the interaction region at the cavity focus. The pulse electric field E is determined from the NLSE as:

$$\frac{\partial E}{\partial z} = -i\frac{k''}{2}\frac{\partial^2 E}{\partial t^2} + ik_0 n_2 |E|^2 E - \frac{W(|E|^2)U_i}{2|E|^2}(\rho_0 - \rho) \tag{4.1}$$

where the first term on the right hand side incorporates the linear temporal dispersion due to propagation through a medium with group velocity dispersion coefficient k''. The second term is the instantaneous Kerr response of the gas with n_2 being

the nonlinear index of refraction and k_0 the vacuum wavenumber. The final term describes the response of the pulse electric field to the generated plasma with U_i being the ionization potential of the gas and ρ_0 the neutral atomic gas density. The photoionization rate $W(|E|^2)$ was obtained from the generalized Keldysh-PPT formula [27, 68].

The model uses the Split-Step Fourier Method to solve the NLSE by propagating an 80 fs pulse through the xenon gas jet. After propagation through the interaction region, the cavity transfer function is applied by multiplying the pulse electric field $E(\omega)$ by the cavity transfer function $T(\omega)$ and then adding the input pulse to the circulating field. This process is repeated until a steady-state solution is obtained. The cavity transfer function is given by

$$T(\omega) = (1 - L)e^{i\Phi_{RT}} \tag{4.2}$$

where L is sum of all cavity losses and Φ_{RT} the total round trip phase shift. Linear dispersion in the cavity is incorporated into Φ_{RT} as a power expansion:

$$\Phi_{\mathrm{RT}} = \Phi_0 + \Phi_1(\omega - \omega_0) + \Phi_2(\omega - \omega_0)^2/2 + \Phi_3(\omega - \omega_0)^3/6 + ... \tag{4.3}$$

with ω_0 being the center wavelength of the cavity mirrors and Φ_n the mirror dispersion coefficients. When the pulse train is optimally matched to the fsEC, Φ_0 and Φ_1 are set to 0 as these affect only the round trip carrier phase and group delay. The parameters Φ_2 and Φ_3 are the second and third order dispersion coefficients respectively.

Estimated experimental values of $\Phi_2 = -5 \pm 5\mathrm{fs}^2$, $\Phi_3 = 600 \pm 200\mathrm{fs}^3$, and $L = 0.8 \pm 0.1\%$ were used in the calculations for our fsEC with a 0.5% input coupler. Small variations of these parameters within the given uncertainties were tested and do not severely affect the main features exhibited in the simulations. The largest uncertainty in the experimental parameters is the gas jet density and interaction length at the intracavity focus. Fluid flow simulations suggest that it is reasonable to predict a pressure drop of 10 to 20 times that of the backing pressure, changing rapidly with

distance from the gas nozzle [69, 60]. Similarly, an interaction region of 400 μm is used for the 300 μm wide nozzle opening due to the rapid expansion of the jet.

4.2.2 Plasma Decay Rate

In addition to the pulse electric field, the model must also account for variations of the plasma density. Plasma is generated during the most intense portion of the pulse and decays over time scales much longer than the pulse duration but on the same order as the pulse round trip time.

There are multiple possible mechanisms that can lead to an effective decay of the plasma within the pulse interaction region. First, because the gas is delivered at a certain flow rate, there is a finite amount of time an atom will remain within the interaction region. For typical fsEC conditions this is expected to be about 60-80 ns and should exhibit a nearly linear decay rate [70]. For repetition rates around 100 MHz, this corresponds to about six cavity round trips and probably only has a small effect on the observed dynamics.

Additional mechanisms leading to lower plasma densities in the fsEC include radiative electron-ion recombination, three-body recombination, and ambipolar diffusion [71]. In the numerical model used here, radiative recombination is assumed to be the dominant mechanism though we note that the other factors listed in this section may contribute. Furthermore, for the purposes of our 1D model, the important parameter was not the actual decay rate that was chosen but rather the density of plasma remaining after one round trip. For more discussion on this decay, see Section 4.3.3 describing a direct pump-probe measurement of the plasma decay rate.

Thus in our model, using the Keldysh-PPT formalism for the ionization rate $W(|E|^2)$ and radiative recombination as the decay mechanism, the electron plasma density ρ evolves in time as

$$\frac{\partial \rho}{\partial t} = W(|E|^2)(\rho_0 - \rho) - \alpha\rho^2 \tag{4.4}$$

where α is the plasma recombination coefficient with units of [cm^3/s].

4.2.3 Simulated fsEC line shapes

In order to enable direct quantitative comparisons to the experiment and to remove the uncertainties with the active cavity stabilization, the fsEC resonant lineshapes were simulated using the 1D model described above. These lineshapes are obtained experimentally by scanning the cavity length using a PZT mounted mirror at a rate of 5 GHz/s and monitoring the transmission through one of the cavity mirrors with a photodiode. The dashed line in Figure 4.2(a) shows a typical lineshape for an empty cavity revealing a smooth, symmetric, Lorentzian profile. When gas is introduced at the cavity focus, the lineshape becomes strongly distorted depending on the degree of ionization and the fsEC parameters. Figure 4.2(a) shows a sequence of experimental lineshapes for xenon backing pressures up to 300 Torr revealing that the maximum pulse energy enhancement occurs at slightly detuned frequencies ($\Delta \neq 0$) relative to the linear cavity case.

The simulated lineshapes in Figure 4.2(b) agree well with the experimental curves obtained in (a) with only the gas pressure and plasma recombination coefficient α used as fitting parameters. The maximum pulse energy occurs at a detuning of Δ_p and is shown by the dotted vertical line in Figure 4.2(b) and occurring at $\Delta_p = 61$ kHz for an actual target pressure of 20 Torr.

If the cavity is scanned in the opposite direction, such that the phase shifts from the length change and the plasma have different signs, the nonlinear line shapes in the two directions look different. This is shown in Figure 4.3 and reveals that the cavity is bistable in the presence of strong ionization. This means that near the cavity locking point (black arrow in figure), a small perturbation could cause a shift to the lower energy line shape. Such a shift would cause the cavity resonance condition to change due to the reduced plasma density at the focus and can lead to oscillations

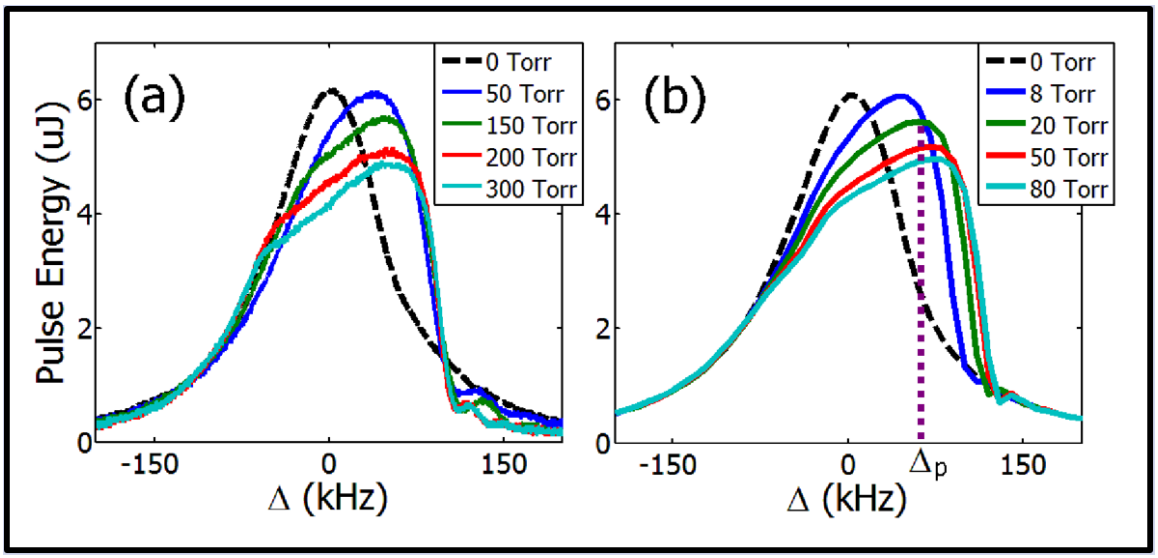

FIGURE 4.2. (a) Experimental fsEC line shapes for various target gas pressures and at vacuum (dashed line). (b) Simulated line shapes showing actual target gas pressures used. The vertical dotted line shows the detuning Δ_p at which the maximum energy enhancement occurs for the case of 20 Torr gas pressure.

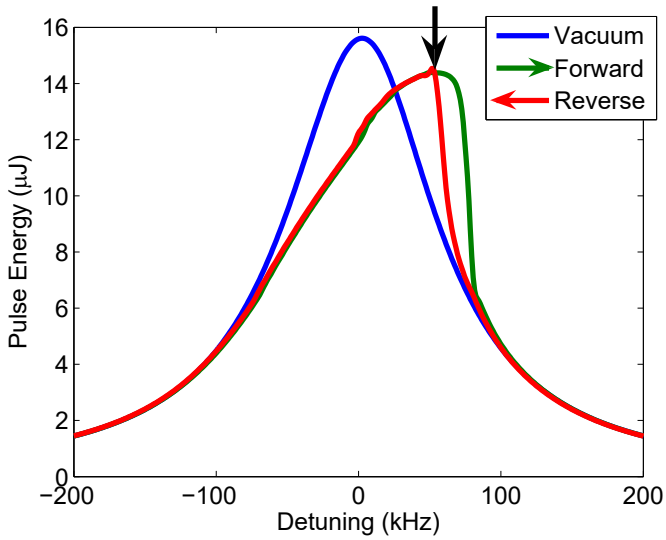

FIGURE 4.3. Comparison of fsEC line shapes obtained at vacuum (blue) versus scanning in the positive (green) and negative (red) frequency directions in the presence of intracavity ionization. Near the servo locking point (denoted by black arrow), a bistable region is observed in which small deviations about the lock point could cause a drop to the lower power line shape. Such behavior can lead to instabilities in the cavity lock.

in the intracavity power as the servo tries to compensate (see locking instability in Figure 4.1). One way to minimize the effects of this instability is to shift the lock point down from the peak of the deformed lineshape to a point where both curves overlap [70]. An additional approach to reducing this effect is to increase the input coupling percentage. For example, with recent advances in fiber laser technology, output powers greater than 100 W are now achievable and with an input coupling percentage of 1.5% or more it is still very easy to reach ionization intensities inside the cavity.

The simulations also reveal that the value chosen for α strongly affects the line shape and position of Δ_p. Furthermore, the line shapes can *only* reproduce the experimental curves for the proper value of α. We found that the best results were obtained for $\alpha = 2 \times 10^{-9}\text{cm}^3/\text{s}$. Because α determines the amount of plasma remaining after one round trip, a constant phase shift is seen by the pulse on each pass through the cavity, similar to what would be seen by a change in the cavity length. These results were published in 2011 and showed for the first time that a residual background plasma existed in the fsEC and was a limitation to the overall system performance [72].

It is the background plasma effect that is responsible for the bistability described above and, as mentioned in Section 2.2.2, it is also detrimental to HHG phase matching. As a result, it is highly advantageous to find ways to minimize the amount of residual plasma seen after a round trip. Reducing the laser repetition rate is one way to accomplish this as there is more time between pulses for the gas to transit the interaction region. It may also be possible to increase the flow rate by using an improved nozzle geometry, heating the xenon, or seeding it with a lighter element such as helium. Indeed, it has been reported that a mixture of helium and xenon lead to an increase in harmonic yield of 30% over a pure xenon target [42].

4.2.4 Steady-State Characteristics

In addition to studying the cavity line shapes, the model was used to understand both the pulse build-up and the steady state behavior. In the absence of the gas jet, the pulse evolves to a steady-state solution with a total energy limited only by the cavity losses and dispersion as described in Section 3.1.1. The input pulse parameters are fixed to yield a maximum intracavity build-up at low energy ($\Delta = 0$). At high pulse energies in the presence of the target gas, the pulse acquires a nonlinear phase shift as the peak intensity reaches the ionization threshold of the gas. This phase shift, shown in Figure 4.4(b), changes across the pulse profile and reduces the constructive interference with the incident pulse train. As a result it introduces a fundamental limit to the achievable pulse energy enhancement in the fsEC. This effect can be seen clearly in plots of the temporal pulse profile shown in Figure 4.4(a). The non-zero phase shift on the leading edge of the pulse is due to the static background plasma that does not completely decay away during a complete round-trip time. Just before the pulse center at $t = 0$, the phase shift trends positive due to the nonlinear Kerr effect becoming significant but quickly goes negative as the pulse intensity becomes high enough to ionize the xenon target. As the gas pressure, and consequently the plasma density, is increased, the growing nonlinear chirp of the pulse causes the peak intracavity intensity to drop.

These results demonstrate that even if the nonlinear shift of the cavity resonance is compensated by the active servo stabilization, it will not be possible to achieve the same intracavity energy enhancement obtainable at low powers. Instead, as the incident pulse energy is increased, the enhancement ratio will drop though the total intracavity pulse energy will continue to grow.

The 1D model described here only takes into account propagation along the laser axis, however potential spatial effects were taken into account in a separate quasi-cw 3D model. In this separate model, developed by John Mongelli for his master's thesis,

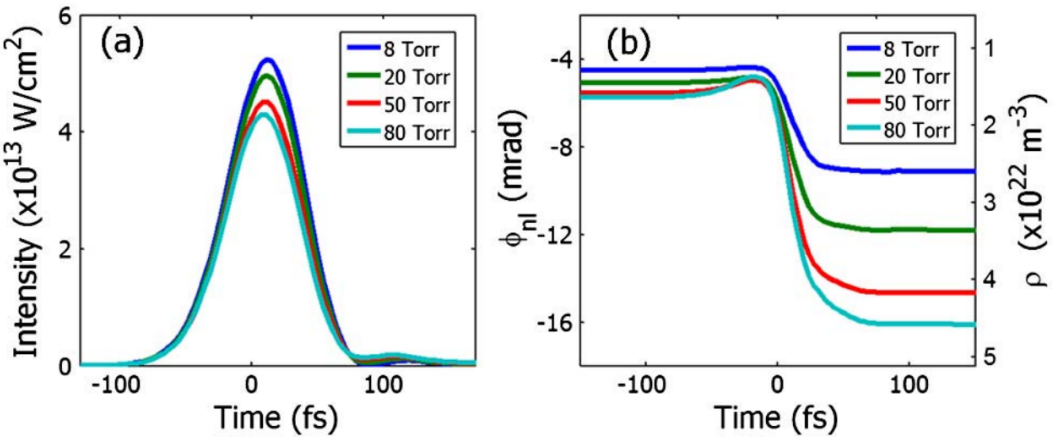

FIGURE 4.4. (a) Steady-state intracavity pulse profile and (b) nonlinear phase shift (with corresponding plasma density) for various target gas pressures. The offset on the leading edge of the pulse (left side of graph) is due to the static background plasma that does not decay away after one cavity round trip. Just before $t = 0$, the phase shift moves in the positive direction indicating the effect of the instantaneous Kerr response. Near $t = 0$, the peak intensity is at its maximum and the negative phase shift due to ionization of the gas dominates. The long lifetime of the plasma means that this phase shift accumulates across the latter part of the pulse profile and slowly decays over the cavity round-trip time.

the temporal structure of the pulse was kept constant but spatial effects were included by incorporating a nonlinear phase profile in the x and y dimensions [73, 74]. The spatial phase profile was calculated from a single-pass propagation through the gas jet region for a range of peak pulse intensities. The results were tabulated and allowed the proper phase shift to be applied on each cavity round trip. After applying the nonlinear phase shift, the field was propagated around the cavity using the generalized Huygen's integral [43] which allows different ABCD matrices to be used for the two transverse directions in order to account for cavity astigmatism. Iterating the field around the cavity yields a steady state beam profile and peak intensity that was then compared to the 1D time-resolved model.

Figure 4.5 shows line shapes obtained from the two models. We found that there is good agreement when the nonlinear phase shift in the 1D model is scaled by a constant geometric factor of 0.46. This scaling factor arises from the fact that the transverse beam profile and electron density profile are not identical. Because the electron density profile is narrower, this leads to an overestimate of the nonlinear phase shift in the 1D model. By applying this correction factor to the 1D model, most of the fsEC behavior in the 3D model is captured. This means that the cavity remains predominantly in a single transverse mode and thus it is reasonable to use the 1D model of Equations 4.1 and 4.4 to include cavity dispersion and other relevant temporal dynamics.

Figure 4.6 shows the intracavity peak intensity as a function of round trip number and demonstrates how the nonlinear chirp acquired by the intracavity pulse leads to a reduction in intracavity power. If the cavity resonance is fixed at $\Delta = 0$ kHz, where the maximum energy is obtained in the absence of a target gas, the intracavity energy is clamped at a much lower value than obtained in the empty cavity. However, in the experiment the servo loop will be able to follow the resonance shift if the effect is not too strong, thus compensating for some of this reduction in intensity. To gain insight into this process, we simulate a slow shift of the resonance towards a detuning of Δ_p

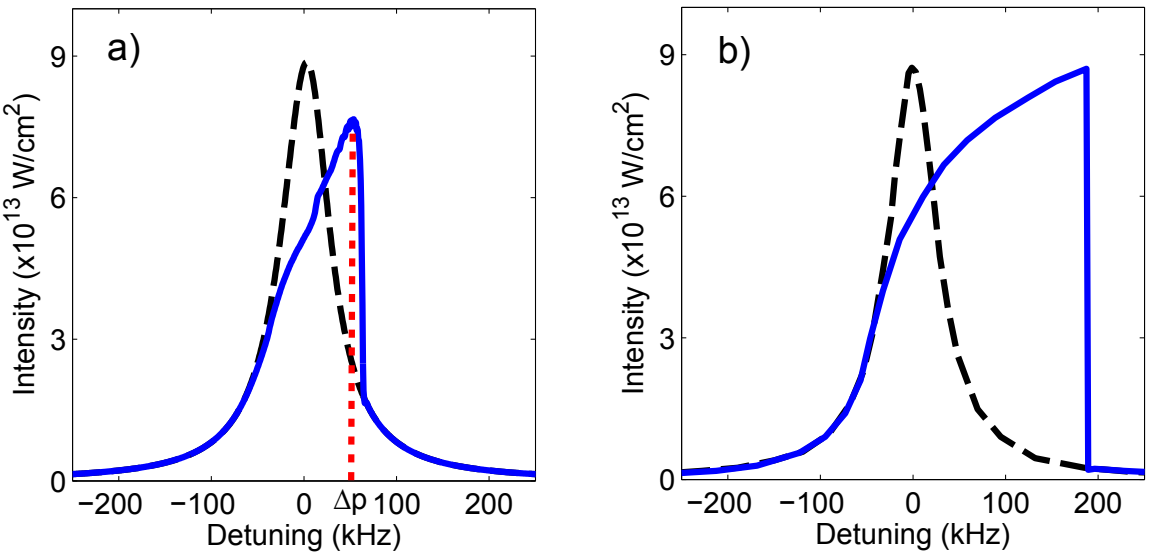

FIGURE 4.5. Comparison of line shape profiles for the a) 1D temporally resolved model and b) the quasi-cw 3D model. A strong shifting of the cavity resonance is observed in both models but only the time-resolved model captures the reduction in intracavity intensity due to the nonlinear chirp acquired by the circulating pulse. Both simulations used an incident pulse energy of 75 nJ, a 0.5% input coupler, and 0.3% round-trip cavity scattering losses. The dotted vertical line in a) marks the detuning Δ_p at which the fsEC is maximally resonant in the presence of ionization under these conditions.

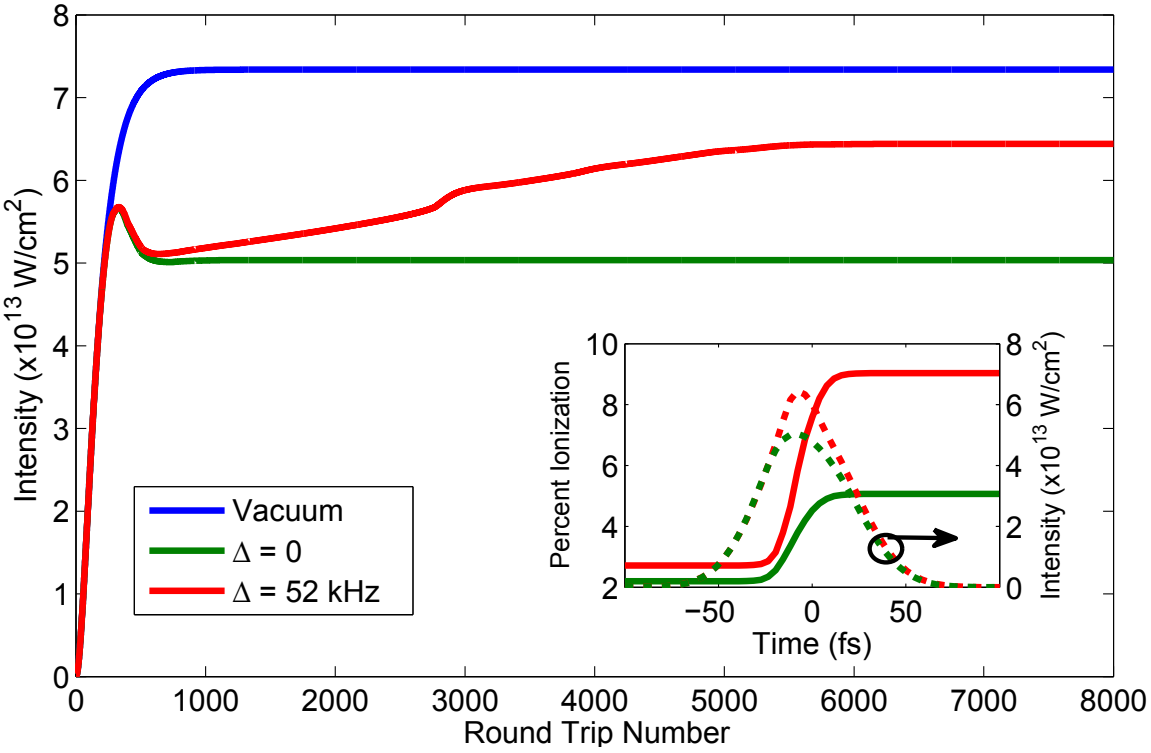

FIGURE 4.6. Build-up plot of intracavity peak intensity versus round trip number for linear cavity (blue), cavity length fixed at $\Delta = 0$ kHz, and cavity length scanned to $\Delta_p = 52$ kHz. The inset shows the corresponding pulse profile and xenon ionization fraction versus time.

as shown in Figures 4.5 and 4.2. While this is not a true simulation of the active feedback loop it reveals how much intracavity energy can be recovered relative to the empty cavity case. The difference in buildup between the $\Delta = 0$ and $\Delta = 52$ kHz cases is due to the static background plasma and shows that if this can be minimized, the servo loop does not have to work as hard to maintain resonance.

4.3 Pump-Probe Phase Measurement

4.3.1 Basic Principles

The numerical simulations described in the previous section showed that a fundamental limit to intracavity HHG systems stems from the plasma dynamics at the cavity focus [72, 70]. However, the line shape comparisons in those simulations did not provide a direct measurement of the plasma density nor did it yield any information on the plasma decay rate. To address these issues, we demonstrated a novel technique for measuring the plasma density and decay in real-time using an fsEC with two independent frequency combs in a counter-propagating pump-probe geometery. A schematic of this system (with Brewster window removed) is shown in Figure 4.3.1 with a high power "pump" beam coupled into the fsEC in one direction and a low power "probe" beam in the opposite direction. The probe power is kept to a few mW to eliminate any nonlinear contributions from the probe itself and passes through a 13 MHz EOM in order to generate a PDH error signal that can be used as a phase-calibrated reference. If the two combs are tuned to have slightly different repetition rates, the pulse delay is continously scanned over the maximum delay determined by the repetition rate of the laser. The *rate* at which this delay is scanned is determined by the difference in repetition frequencies of the two combs.

When the strong pump pulse ionizes the target gas, a plasma is formed that induces a linear phase shift for the weak probe pulse that follows. The strength of this phase shift is determined by the amount of plasma seen by the probe at the given delay and is observed in the probe error signal as a frequency shift of the cavity resonance.

The phase shift arises from a modification of the local refractive index in the gas jet due to the plasma generation. The frequency-dependent index of refraction of a

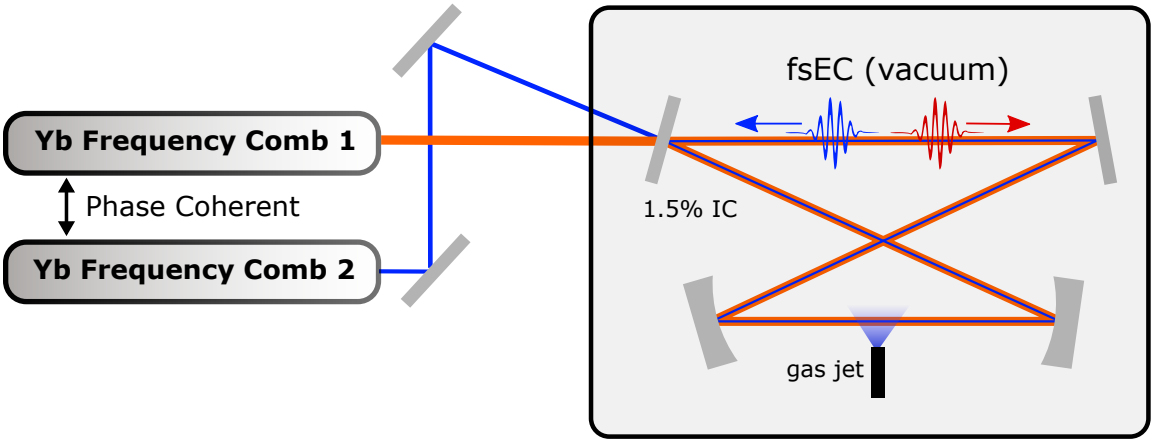

FIGURE 4.7. Schematic of the fsEC pump-probe system for measuring the intracavity plasma. Two independent frequency combs with slightly different repetition rates are coupled to the fsEC in a counter-propagating geometry. The weak "probe" laser sees a phase shift induced by the pump due to the background plasma density. This phase shift is observed on the probe error signal as frequency shift of the cavity resonance.

plasma is given by

$$n(\omega) = \sqrt{1 - \frac{\omega_p^2}{\omega^2}} \tag{4.5}$$

$$\approx 1 - \frac{\omega_p^2}{2\omega^2} \tag{4.6}$$

where ω_p is the characteristic plasma frequency. The value of ω_p is determined by the electron density n_e and can be expressed as

$$\omega_p^2 = \frac{n_e e^2}{\epsilon_0 m_e} \tag{4.7}$$

with e and m_e being the electron charge and mass respectively and ϵ_0 the vacuum permittivity constant.

The phase shift $\Delta\phi$ on a pulse with center wavelength λ propagating through the gas jet of length l is thus

$$\Delta\phi = k_{\text{gas}} l - k_{\text{plas}} l = \frac{2\pi l}{\lambda}(\Delta n). \tag{4.8}$$

By measuring the intracavity phase shift of the probe pulse it is possible through Equations 4.5 and 4.8 to calculate the actual plasma density in the interaction region. Experimentally this is done by applying a small modulation to the probe laser with an EOM to generate a PDH error signal as described in Section 3.1.3. The central linear region of the error signal is phase-calibrated from the sideband peaks in the linear cavity line shape. Thus, when the cavity is locked, the probe error signal exhibits a dc offset proportional to the plasma density it encounters at a given delay. The utility of this method is that it allows us to characterize in a fully time-resolved manner the nonlinear phase shifts that typically limit IHHG experiments.

4.3.2 Single-Comb Results

The line shapes computed in the previously described numerical simulations were revisited using the pump-probe setup. If both the pump and the probe are set to have identical repetition rates, they can be scanned simultaneously across the cavity resonance. This was initially performed using the Ti:sapphire system from Section 3.2 and since both the pump and probe were derived from the same laser, each had the same repetition rate. The probe pulse in this configuration was delayed with an adjustable mechanical delay line. The line shapes obtained simultaneously for the pump and probe are shown in Figure 4.8. As expected, in the absence of any target gas, both the pump and the probe show the same linear cavity response. However, once the gas jet is turned on, the two combs effectively see very different enhancement cavities. At very short delays ($\tau < 1$ ps), the strong plasma seen by the probe causes a strong shift of the cavity resonance beyond that supported by the "pump cavity". This results in a sharp spike near the falling edge of the pump line shape on the right side of the figure. As the delay τ is increased, this shift relative to the peak of the pump line shape shifts to the other side of the resonance, indicating a lower level of plasma.

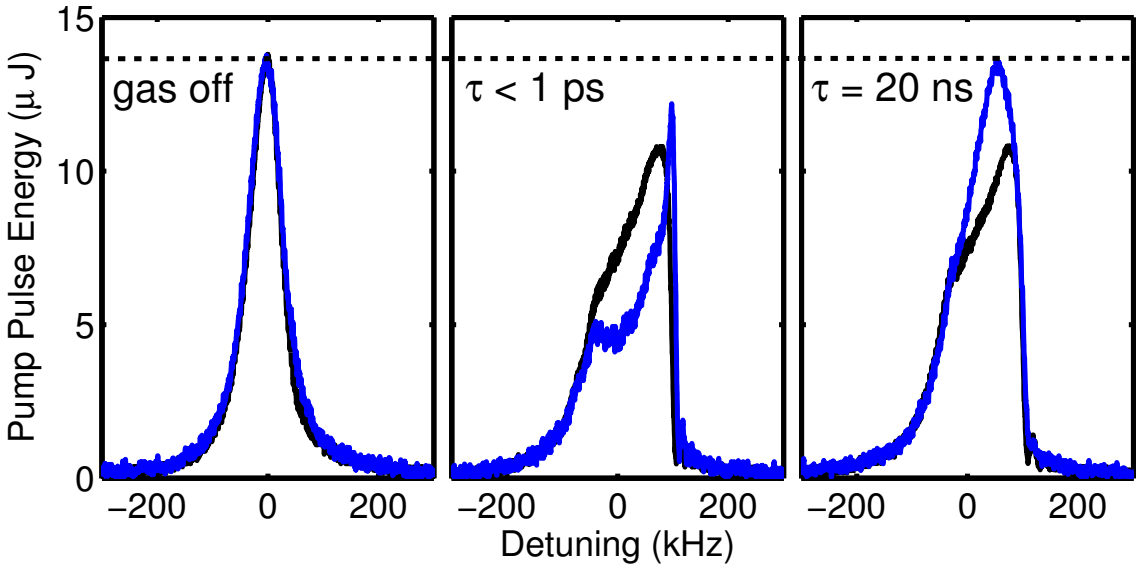

FIGURE 4.8. Pump (black curve) and probe (blue curve) line shapes as the cavity length is scanned through resonance. In the left panel there is no gas and each beam sees the linear empty cavity resonance. The central panel shows the line shapes with 100 torr Xe and a short delay between the pump and probe pulses. The lineshapes at the maximum possible delay of 20 ns are shown on the right.

Unfortunately it is difficult to infer any quantitative information from the probe line shapes because they are obtained at the same time as the pump is scanned through resonance. Furthermore, with only a single comb source, the mechanical delay that must be used is very restrictive in the delays that can be reached.

4.3.3 Two-comb results

In addition to being able to pursue dual comb spectroscopy in the VUV, the two Yb fiber lasers in Section 3.3 allowed us to do a more sophisticated pump-probe measurement than we could with just a single laser source.

Figure 4.9 shows the probe phase shift as a function of delay for various xenon backing pressures. Because the probe error signal shows the shift relative to the pump resonance, the dc offset in the figure representing the static background plasma cannot be obtained directly. To get the background level, the pump laser was frequency-modulated at 70 kHz and a lock-in detection scheme was used on the probe error signal at the same frequency. This modulation was fast compared to the servo bandwidth to avoid coupling through the intracavity PZT but slow relative to the cavity round trip time. The two lasers are coupled only through the plasma and the relative offset from zero in the probe lock-in signal provides the background shift. This was verified experimentally by the fact that no 70 kHz modulation was seen on the probe error signal in the absence of ionization in the cavity. For each curve in the figure, a nearly linear decay in the phase shift is observed over the maximum delay range. This linear reduction in plasma density provides strong evidence that neither three-body recombination nor radiative recombination alone are the dominant decay mechanisms when using end-fire nozzles in IHHG systems. Furthermore, there is a significant fraction that persists as a constant background at all tested pressures, in agreement with the numerical simulations described in Section 4.2. Since the constant background in the interaction region is so problematic for IHHG experiments,

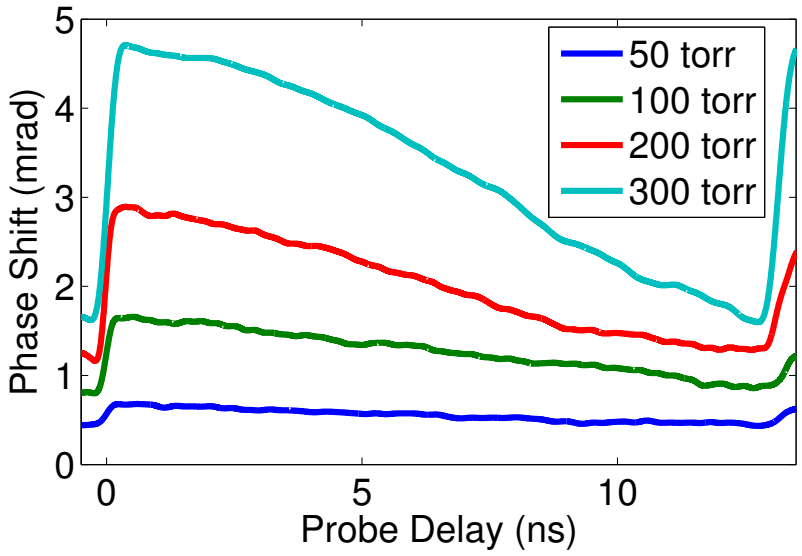

FIGURE 4.9. Decay of intracavity plasma as a function of probe delay. The rate of decay is observed to vary with backing pressure though a significant background level persists for all pressures tested.

having a technique like the one described here will allow for the testing of strategies to minimize it and improve the robustness of the cavity stabilization.

An alternate measurement was taken in which the xenon backing pressure was fixed at 38 Torr and the intracavity power was varied by changing the incident laser power with a half-waveplate and polarizing beamsplitter combination. The results are plotted in Figure 4.10 with the probe phase shift normalized to unity at $t = 0$ when the pulses overlap in the gas jet. The observed decay at later times then represents the fraction of plasma remaining as seen by the probe. While the slopes of these curves remain nearly linear, an intensity-dependent change in the rate is seen. This shows that some plasma density dependent process is contributing to the decay and the observed effect is not simply due to the ionized particles transiting the interaction region.

As mentioned previously in Section 4.2.2, there are multiple ways in which the

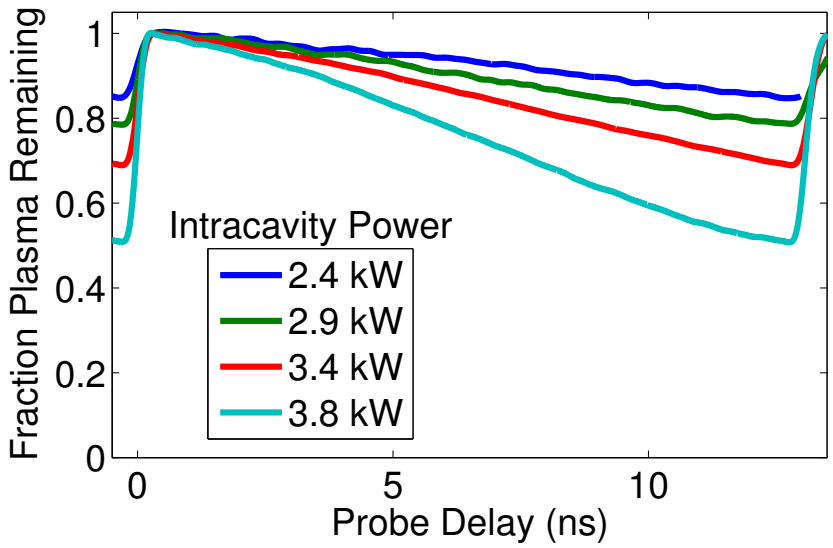

FIGURE 4.10. Fractional plasma decay as a function of probe delay for various intracavity power levels. The decay rates are normalized to one at $t = 0$ to show the relative decay rates. While the decay slopes are linear, they exhibit an intensity-dependent slope, implying that higher initial plasma densities lead to faster decay rates.

plasma can decay or otherwise leave the interaction region. If an electron collides with an ion it can recombine into a neutral atom but, in order to conserve momentum, a third body must be present. If the third body is another electron, this process is called "three body recombination", and if it is an emitted photon, it is called "radiative recombination". If the plasma is formed in a neutral gas, the densities of ions and electrons are equal and leads to a time decaying plasma density ρ given by $\partial\rho/\partial t = -\alpha_{\text{3body}}\rho^3$ for three-body recombination and $\partial\rho/\partial t = -\alpha_{\text{rad}}\rho^2$ for radiative recombination where the α values are the respective recombination coefficients.

An additional mechanism that may contribute to the observed behavior is called ambipolar diffusion. As the name suggests, this is not a recombination effect but rather a diffusion process in which the plasma expands and electrons leave the cavity interaction region. When the laser ionizes the xenon target, energetic electrons are liberated from their parent atoms and will tend to diffuse away from the focus. However, this motion creates a small charge gradient as the positively charged ions are left at the center. The resulting electric field "pulls" the ions out of the focus and leads to an overall spatial expansion of the plasma in time. A plasma decaying by ambipolar diffusion will have a density that evolves according to:

$$\frac{\partial\rho}{\partial t} = -D_a\frac{\partial^2\rho}{\partial x^2}. \tag{4.9}$$

where D_a is the ambipolar diffusion coefficient. D_a varies linearly with electron temperature T_e and has a functional form $D_a \propto T_e/\rho_0$ when the relatively small ion temperature is neglected. For a textbook description of ambipolar diffusion see Chapter 5 in Ref. [71].

A plot of these different decay mechanisms is shown in Figure 4.11 compared to an experimentally obtained curve. Each is normalized to one at $t = 0$ and decays to the same fractional value after one round trip time ($t = 12.6$ns). The strong density-dependence of the radiative and three-body recombination curves leads to a fast initial reduction of the density but slows at later times. On the other hand, decay

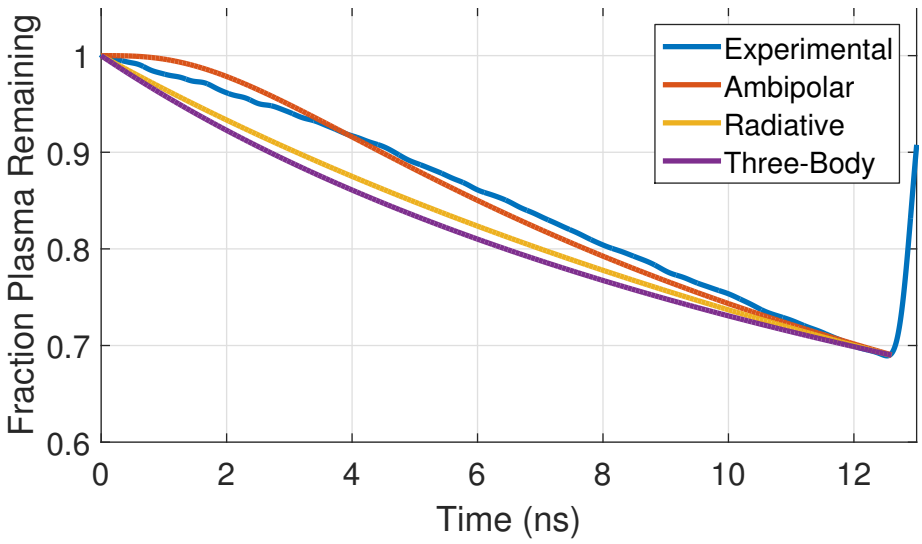

FIGURE 4.11. Comparison of plasma decay rates by various mechanisms. Each curve is normalized to one at $t = 0$ and decays to the same fractional value after $t = 12.6$ ns.

due to ambipolar diffusion does not depend on the initial plasma density but rather on the initial spatial distribution of the plasma which is assumed to have a flat-topped Gaussian profile. Dissipation of the plasma due to ambipolar diffusion should scale linearly with electron temperature which agrees qualitatively with the observed trends in Figure 4.10. However, the data may be best explained as a combination of three-body recombination at early times when the density is highest and transitioning to a diffusion-dominated decay as the density is reduced. However, further study of these effects are required to make definitive statements about the relative contributions of each process.

In addition to characterizing the intracavity plasma, the pump-probe technique described in this section can be applied more generally to any optical nonlinearity in the cavity. For example, Figure 4.12 shows the phase shift of the probe as the delay is scanned through both the cavity focus and the sapphire plate output coupler for the high harmonics. With this approach it is possible to see in a single scan both the

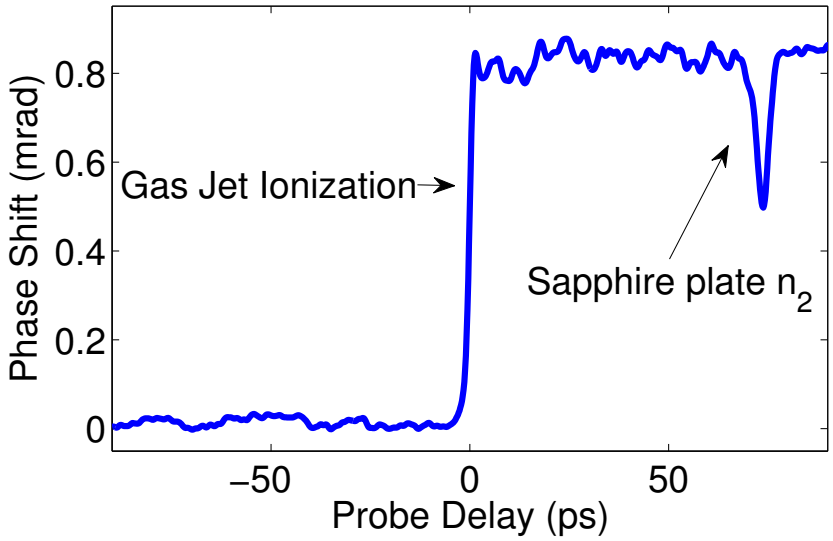

FIGURE 4.12. Probe phase shift near cavity focus showing both the phase shift due to ionization and the instantaneous Kerr response when both the pump and probe pulses are overlapped in the sapphire plate.

long-lived ionization phase shift as well as the instantaneous Kerr response when the pump and probe are overlapped in the sapphire plate. Since the nonlinear refractive index of sapphire is well-known, it may be useful to use this type of measurement as a means to precisely calibrate the peak intracavity intensity. Furthermore, it may also be possible to use this technique to probe nonlinearities at mirror surfaces to investigate damage mechanisms or thermal effects *in situ*.

4.4 Probing the Intracavity Plasma with High-Order Spatial Modes

The previous section discussed ways to probe the time dynamics of the intracavity plasma but it is also interesting to consider the spatial dynamics. To investigate this possibility, we used the higher order Hermite-Gaussian spatial modes supported by

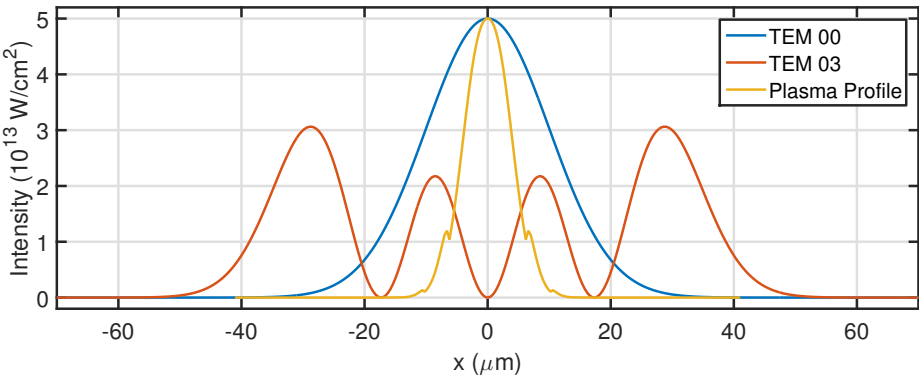

FIGURE 4.13. Plot of transverse spatial profile of the fundamental TEM_{00} cavity mode and TEM_{03} mode at the cavity focus. The intensity axis is calibrated for the TEM_{00} mode which produces a plasma density profile as shown by the yellow curve.

the enhancement cavity. The spatial intensity distributions of these transverse modes (designated TEM_{mn}) with indices m and n are given by

$$I_{mn}(x,y) = I_0 \left[H_m\left(\frac{\sqrt{2}x}{w}\right) \exp\left(\frac{-x^2}{w^2}\right)\right]^2 \left[H_n\left(\frac{\sqrt{2}y}{w}\right) \exp\left(\frac{-y^2}{w^2}\right)\right]^2 \tag{4.10}$$

where I_0 is the peak intensity, H_i is the i^{th} Hermite polynomial, and w is the Gaussian beam spot size [43].

In normal operation, enhancement cavities are operated using the fundamenal TEM_{00} mode but it is possible to couple to the higher order modes as well. Higher order modes of the form TEM_{0X} where x is a positive odd integer have a larger horizontal spatial profile than the TEM_{00} mode and have zero on-axis intensity. For example, the spatial profiles of the TEM_{00} and TEM_{03} modes are shown in Figure 4.13 along with the plasma profile associated with the intensity distribution given by the TEM_{00} mode. This difference in overlap between modes can be exploited in the fsEC to measure spatial variations of small phase shifts due to the neutral gas, the plasma, or thermal nonlinearities, for example.

In Figure 4.14 we measure the difference in resonance frequency between a cw laser coupled to the TEM_{03} mode of the cavity and the TEM_{00} mode as the comb

"pump" laser power is increased. The cw laser is passed through an AOM to allow manual optimization of the resonance frequency by monitoring the intracavity power. When xenon is introduced at the focus at a backing pressure of 50 Torr, there is a shift of about 10 kHz between the two modes at low pump powers. This occurs due the slightly different density profile of neutral xenon gas across the mode profile for the two beams. As the incident pump power is increased, a linear shift is observed for both the empty cavity and 50 Torr Xe curves. This effect is the result of localized bulging on the cavity mirror surface due to thermal heating from the high power intracavity field [75]. Because the TEM_{03} mode has a larger area than the TEM_{00} mode, it does not see the same phase shift. This leads to a consistent correction that must be applied to keep the TEM_{03} mode resonant with increasing pump power. However, once the intracavity intensity becomes high enough to ionize the xenon, the empty cavity and 50 Torr curves cross due to the strong phase shift from the plasma. The plasma has a narrower profile than the TEM_{00} mode (as shown in Figure 4.13) and has comparatively little effect on the TEM_{03} mode.

To compare the degree that the plasma affects the TEM_{00} and TEM_{03} modes, we performed a similar measurement using a fast modulation on the pump beam. The applied 120 kHz modulation is beyond the servo response but can couple to the cw probe beam through the plasma. The modulation of the cw laser error signal is recorded for both the TEM_{00} and TEM_{03} modes as a function of pump power and is plotted in Figure 4.15. At an intracavity power level of 2.7 kW, the response of the TEM_{03} mode to the plasma is approximately 8% that of the TEM_{00} mode. It is expected that even higher order modes would further reduce this percentage.

Because of the reduced spatial overlap with the plasma compared to the TEM_{00} mode, it may be possible to use the TEM_{03} mode to stabilize the cavity length. This approach would be very robust and could remain locked even in the presence of strong nonlinearities. However, for this to work, the thermal resonance shift shown in Figure 4.14 must be compensated. Initial attempts at locking the cw laser to the TEM_{03}

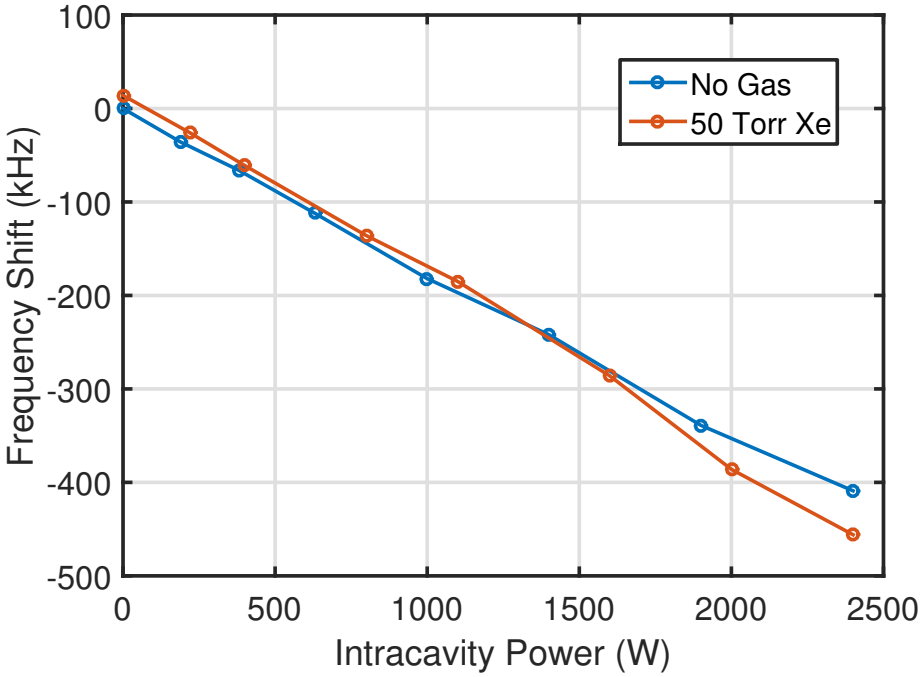

FIGURE 4.14. Resonant frequency shift of a low power cw beam coupled to the TEM_{03} cavity mode relative to the TEM_{00} mode as a function of intracavity power. The blue curve is the shift seen when no gas is present at the focus and the red curve is the shift with a 50 Torr backing pressure of xenon.

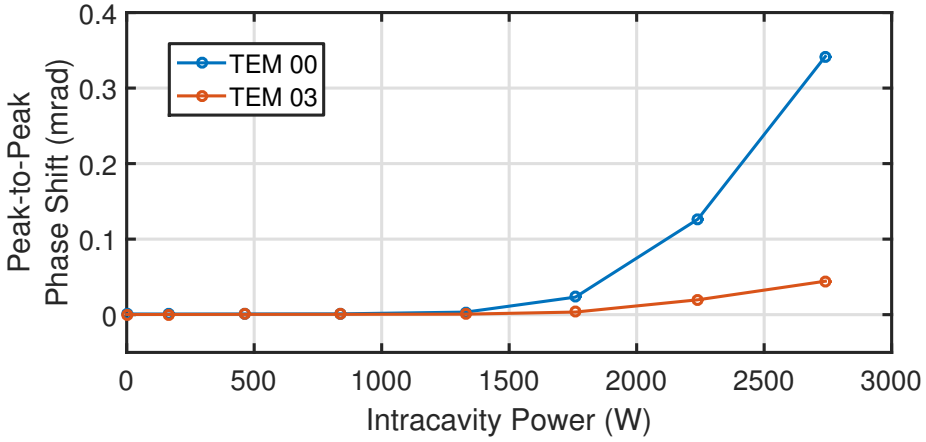

FIGURE 4.15. Peak-to-peak phase shift of the modulation seen by a weak cw laser coupled to the TEM_{00} (blue) and TEM_{03} (red) modes of an fsEC as a function of pump power when xenon is introduced at the cavity focus at a backing pressure of 50 Torr.

mode were unsuccessful because as the pump power was increased, the thermally induced resonance shift would push the cw laser off of resonance. It might be possible to actively stabilize the two modes relative to each other, but it is unclear if this has any significant advantages over directly locking to the TEM_{00} mode. Additionally, it may be possible to use higher order modes to experimentally determine the spatial profile of the gas jet target and plasma profiles directly. This is an area that may warrant further investigation as both better stabilization methods and better understanding of the gas jet dynamics are highly desired.

Chapter 5

Dual-Comb Spectroscopy in the VUV

5.1 Introduction

In the late 1950s, a technique called Fourier Transform Spectroscopy (FTS) was developed based on the standard Michelson interferometer using a broadband incoherent light source [76]. FTS modified the Michelson interferometer by adding an axially movable mirror in one arm, as shown in Figure 5.1, and provided a continuously scanning delay between the two arms. Changing the delay length causes different frequencies of light to interfere constructively at the detector. Thus, over a given period of time, an "interferogram" (IGM) is constructed containing these interference patterns as a function of delay. To reconstruct the source spectrum, a Fourier Transform of this interferogram is computed. The resolution of the spectrometer is thus ultimately limited by the physical mirror displacement which determines the delay time. This technique immediately provided orders of magnitude more resolving power than existing dispersive spectrometers and quickly became a work horse tool of precision spectroscopy [77].

In 2002, a modification of the FTS technique using frequency combs was proposed by S. Schiller and is now called "dual comb spectroscopy" (DCS) [78]. From a conceptual point of view, DCS is very similar to FTS except DCS has the advantage of having no moving parts. The mechanical delay line found in FTS systems is replaced by a continuously scanning pulse delay arising from the differing repetition rates of the comb lasers. The upshot is that IGMs can be acquired faster than in FTS and produce higher resolution spectra due to the ease of scanning through very long de-

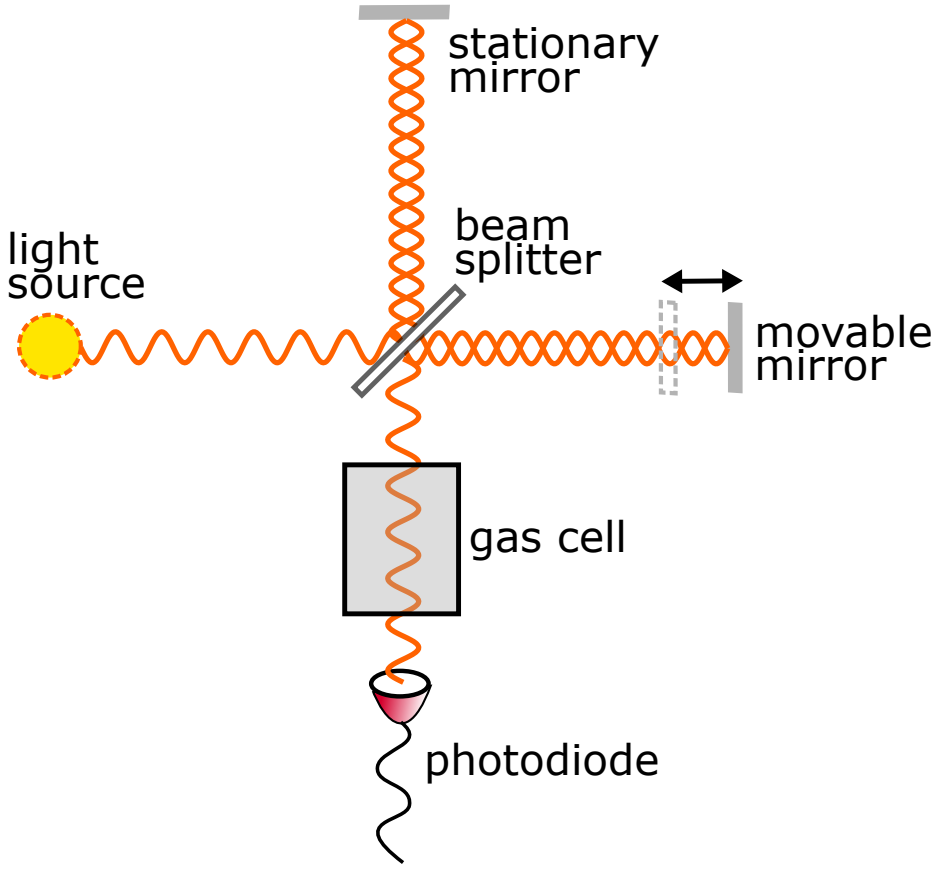

FIGURE 5.1. Basic schematic of the traditional Fourier Transform Spectroscopy technique. A beamsplitter divides a light source into two arms. One arm has a stationary mirror that reflects the light back to the beamsplitter while the other arm contains a movable mirror. As the delay changes, there is constructive interference at the beamsplitter for different frequencies. The resulting "interferogram" recorded by the photodiode contains the spectral information of the source and gas sample and can be retrieved by performing an FFT on the data.

lays. The downside to DCS relative to FTS is that systems can be more complex to construct since they require two separate frequency combs.

Initial experimental demonstrations used unstabilized Ti:Sapphire lasers to achieve optical resolutions of tens of GHz [79, 8]. As a result, it was not possible to resolve individual comb lines. Later, in 2008, Coddington et. al demonstrated DCS using a pair of fully stabilized fiber lasers to achieve an optical resolution of 91 kHz with individually resolved comb linewidths at the Hz level in the RF (limited by acquisition time) [80]. The ultimate resolution of DCS though is not limited by the comb linewidth but rather by the comb line spacing. However it is possible to reach higher resolutions than the line spacing by "interleaving" multiple spectra with shifted comb lines [81].

DCS is a powerful technique providing direct access to the individual modes of a frequency comb. By spatially overlapping two independent frequency combs with slightly different repetition rates ($\Delta f_{rep} \neq 0$), beating is observed between the individual comb components as shown in Figure 5.2. Provided that there is sufficient spectral filtering to avoid aliasing, it is then possible to map each RF beat note to a corresponding comb line in the optical domain. A single DCS measurement can simultaneously provide very high spectral resolution as well as broad bandwidth coverage.

5.2 Laser Stabilization

To maintain phase coherence between the two combs in a DCS configuration, the combs must be actively stabilized with respect to each other. This can be accomplished by locking both f_{rep} and f_{ceo} of each laser directly by providing feedback to actuators in the laser cavities [80], however, complete stabilization in this manner usually requires an f-2f interferometer for each laser [4]. An alternate approach to stabilization is to leave the lasers free running (i.e. no active feedback stabilization)

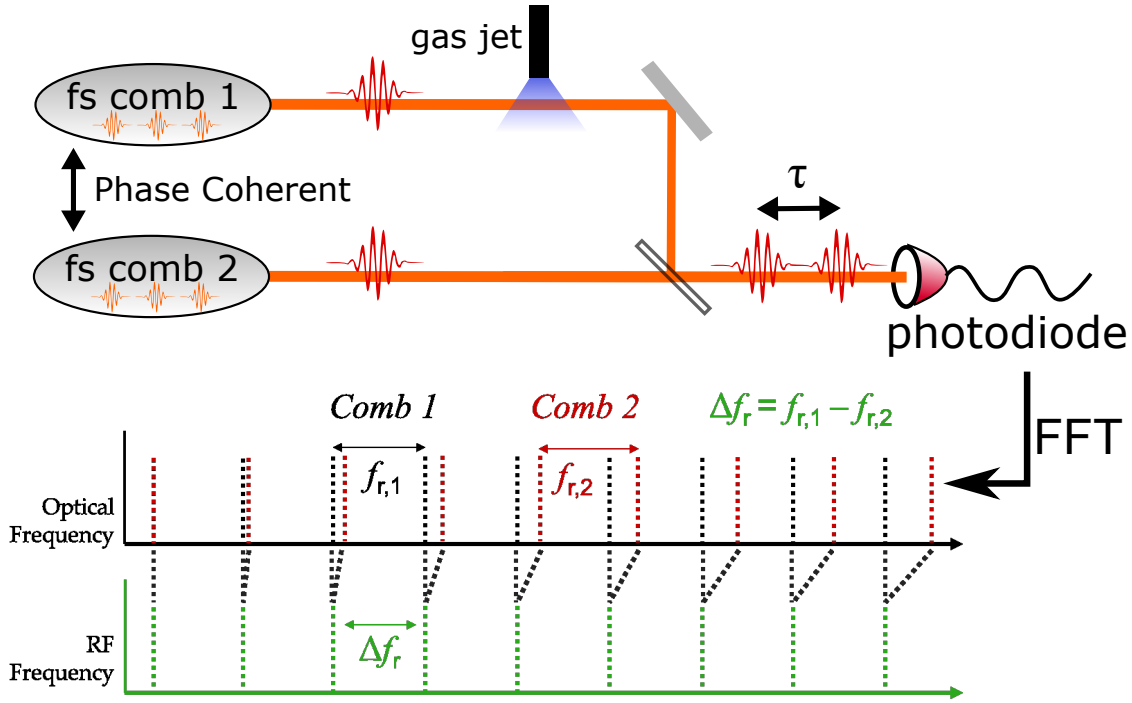

FIGURE 5.2. Diagram of basic dual-comb spectroscopy principle. One comb interrogates a gas sample before being overlapped with the second comb. Time-domain interferograms are recorded with a photodetector and Fourier-transformed to obtain the frequency spectrum. Because the two frequency combs have slightly different repetition rates, the comb modes are down-converted from optical frequencies to the RF. Each pair of comb modes from the two lasers has a unique beat frequency that corresponds to a single optical comb mode.

and use two cw lasers as intermediate frequency references. By recording the drift of beat notes between the cw references and the combs, corrections to the acquired interferograms can be applied to restore the full relative coherence of the two combs. This technique can be applied *a posteriori* using computational methods to correct the relative timing jitter and carrier frequency of the interferograms [82, 83]. Alternatively, the same corrections can be applied using frequency mixing techniques that allow the clock frequency of the acquisition electronics to be adaptively changed [84, 85]. The adaptive technique has the advantage of providing fully stabilized comb spectra in real time with no additional data processing though the system is much less flexible in terms of tunability of the laser frequencies.

In this work, we use a hybrid stabilization scheme combining aspects of direct stabilization and adaptive sampling. Because the combs must remain resonant with their respective fsEC, a purely adaptive approach is not feasible. However, adaptive techniques could be used to post-correct the obtained IGMs to remove any residual noise in the locks. To allow for this type of stabilization, the combs are phase locked to two stable cw lasers at different portions of the comb spectrum. This approach still allows complete control over the comb modes and has additional advantages for locking to an enhancement cavity. Figure 5.3 shows how this technique is implemented in a dual comb experiment. Ideally the two cw laser frequencies lie near opposite edges of the comb spectrum to reduce the effects of additive noise in the comb lines.

Obtaining the two stable cw references is accomplished with the technique described here. The first cw laser (Toptica DL Pro) is tuned to 1070 nm which is near the center of the fsEC spectrum. Locking at this wavelength is optimal because it minimizes amplitude noise in the intracavity power if the second lock has a lower bandwidth. The second cw laser at 1050 nm (Rock fiber laser, NP Photonics) is then locked to the same fsEC as the 1070 nm Toptica laser. This transfer lock stabilizes the two cw lasers with respect to themselves and provides the reference wavelengths for both frequency combs.

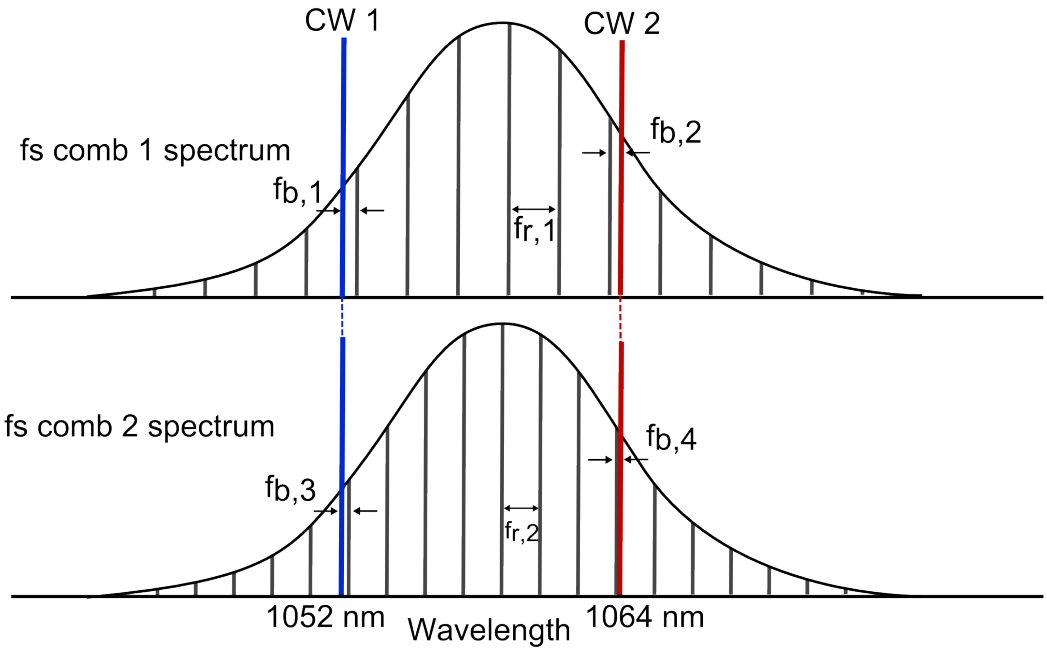

FIGURE 5.3. Dual comb stabilization diagram. Each comb laser is phase locked to two stable cw lasers. Fixing two different modes of each laser allows complete control over the combs.

In this scheme, the cw lasers and fsECs are locked using the PDH technique used in Section 3.1.3. However, the combs are now locked to the cw lasers using optical phase-locked loops. Optical beat notes are obtained by combining the outputs of the cw lasers with the individual combs in a fiber combiner and spectrally filtering the overlapped beams. Amplified InGaAs photodetectors (Electro-Optics Technology ET-3000A, 2 GHz bandwidth) were used to record the beating and RF bandpass filters were used to select a single beat frequency for locking.

One common problem among direct comb stabilization schemes is that the individual actuators in the laser do not provide orthogonal corrections to the two comb degrees of freedom. For example, this may mean that a PZT-mounted mirror does not provide a pure shift of f_{rep} but instead also shifts f_{ceo}. Finding a combination of suitable actuators with high bandwidth and minimal crosstalk can be difficult. For the lasers used in this work, it was found that the best combination involved locking the combs to the 1070 nm Toptica laser using an EOM, pump current control, and long-range PZT in series. The EOM provides locking bandwidths beyond 200 kHz when two differential gain stages are incorporated into the feedback loop. However, the EOM has a very small amplitude response and cannot correct for the large fluctuations at low frequencies. A long-range PZT mounted to a translation stage can provide a large tuning range but at very low bandwidth. In order to correct moderate fluctuations at frequencies beyond 100 Hz, an intermediate servo is used to feedback to the laser's pump current in order to minimize the amplitude range required for the EOM to stay locked. It is important for this first lock at 1070 nm to be as tight as possible since most of the comb noise can be eliminated at this step. The second lock at 1050 nm is done by feeding back to a "tip/tilt" PZT placed behind the grating pair in the laser oscillator. Because the light at this location in the cavity is spectrally resolved, a horizontal tilt of the mirror creates a wavelength-dependent delay. If the tilt is antisymmetric about the center of the beam profile, there is no shift of the cavity length (f_{frep}) to first-order and the only change is in the laser offset frequency

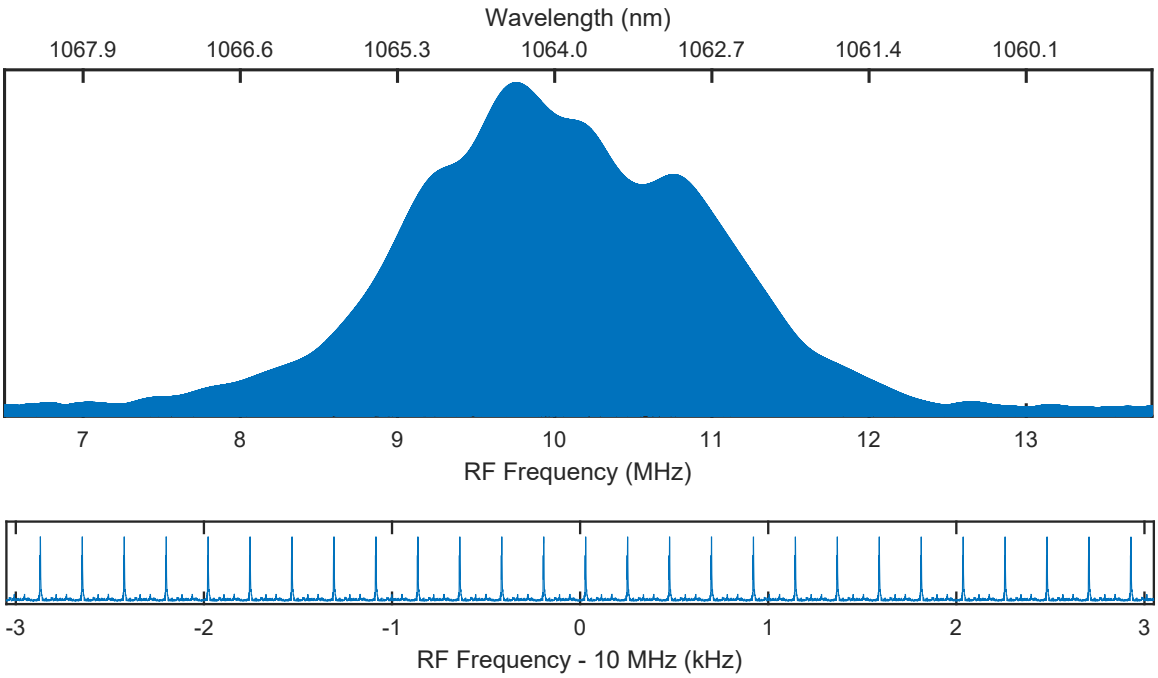

FIGURE 5.4. Typical dual comb spectrum obtained at the fundamental laser frequency plotted as a function of optical wavelength (top axis) and down-converted RF (bottom). The broad optical spectrum of the overlapped comb lasers is optically bandpass filtered around 1064 nm (3 nm FWHM) to avoid aliasing effects in the resulting spectrum. The lower plot is a roughly 1000x zoom of the upper spectrum at the 1064 nm center wavelength. The comb lines are spaced by the repetition rate difference $\Delta f_{\mathrm{rep}} = 223$ Hz.

f_{ceo}. This is accomplished by gluing a small PZT to opposite sides of the mirror and applying corrections of opposite sign to each. The feedback bandwidth of this actuator is approximately 30 kHz.

To demonstrate the effectiveness of the locking scheme, a sample dual comb spectrum was obtained at the fundamental laser frequency outside of the enhancement cavity. The FFT of a 1 sec acquisition is shown in Figure 5.4 at repetition rate difference of $\Delta f_{\mathrm{rep}} = 223$ Hz. The IGMs are optically bandpass filtered around 1064 nm

with a FWHM of 3 nm to avoid aliasing in the spectrum. The lower plot shows an approximately 1000x zoom near the center wavelength to reveal the individual comb modes. The RF comb linewidth is just over 2 Hz and is slightly larger than the 1.2 Hz transform-limited resolution. This shows that there is still some residual noise in the phase locks that could be compensated for with tighter locks or a post-correction technique as mentioned earlier.

5.3 DCS in the VUV/XUV

To perform DCS in the VUV there are two possible experimental configurations: 1) a single fsEC seeded by two independent comb lasers and 2) a separate fsEC for each laser with the harmonic beams overlapped in a separate interferometer. The following sections discuss the relative merits and challenges of each of these approaches.

5.4 Single Cavity DCS

5.4.1 Limitations

The primary advantage to approach 1) in which a single fsEC is used is that the resulting harmonic combs are automatically overlapped and mode-matched. It is very difficult to construct a VUV/XUV interferometer but because the two fundamental combs share the same cavity mode in this configuration, this problem does not exist.

Figure 5.5 shows the schematic for the single cavity DCS experiment. The amplified Yb combs are overlapped with orthogonal polarizations before the fsEC at a polarizing beamsplitter (PBS) and then pass through a half-waveplate and second PBS that forces the two lasers to have the same polarization while allowing tuning of the relatively powers. It is important to note that with this approach, there will be a 50% power loss for each beam when they have equal incident powers. It is also important that the incident laser power and fsEC enhancement are still sufficient to

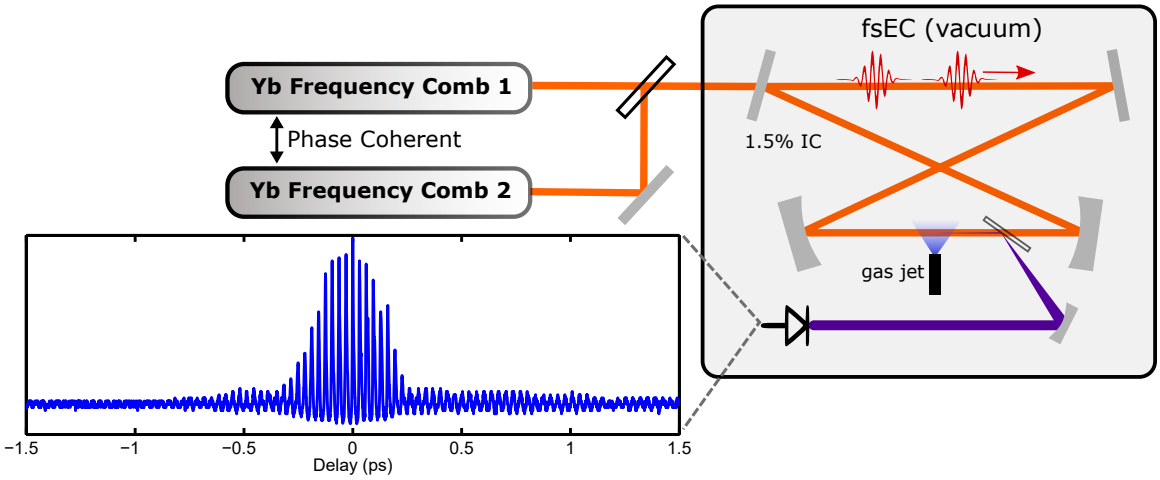

FIGURE 5.5. Schematic of the single cavity dual comb experiment. Two phase coherent frequency combs seed the same fsEC in a co-propagating geometry. In this configuration, nonlinear cross-correlation signals are produced for each of the harmonic orders as shown here for the third harmonic.

ionize the target gas at this reduced power level. Fortunately, this is still achievable with our Yb PCF amplifiers operating at the 50 W level.

While achieving good spatial overlap is not an issue, there are several other challenges that must be addressed in order to successfully implement the single cavity approach. First of all, because the fsEC linewidth is relatively narrow (100 kHz), only small detunings of the repetition rates will be supported by the cavity. For a typical fsEC with a 1% input coupler, the maximum detuning is $\Delta f_{\text{rep}} \approx 5$ Hz in order to still achieve an enhancement factor of 100 (see Figure 3.8 in Section 3.1.4). Performing DCS at these small values of Δf_{rep} leads to relatively long acquisition times, especially for achieving individual comb-mode resolution in the final spectra. The long acquisition time places stricter requirements on the cavity stabilization in order to maintain full phase coherence in the interferograms. A successful implementation of a single cavity DCS system would almost certainly require *a posteriori* correction

of the resulting interferograms as described in [83].

In this configuration the interferograms that are obtained are complicated somewhat by the fact that the fundamental pulses will overlap in the gas jet and produce interference fringes at a frequency of Δf_{rep} and not at $N_{\mathrm{harm}}\Delta f_{\mathrm{rep}}$ as expected for a given harmonic order N_{harm}. This effect has been studied in the context of wave packet interferences in second harmonic generation and leads to interference in the IGMs at the difference of the fundamental frequencies when the two pulses are fully or partially overlapped in the nonlinear medium [86, 87]. Successful recovery of the DCS spectrum would require careful separation of the different frequency components in the overlap region.

An additional problem with using a single cavity is that the pulses will see varying phase shifts as a function of time as they propagate through the decaying plasma. The continuously changing phase shift must be accurately characterized in order to correct the IGMs and reduce artifacts in the final spectrum. It may be possible to use the pump-probe technique described in the previous chapter to measure the needed phase correction. In extreme cases where the ionization level is high, the second pulse to pass through the gas jet will see a reduced number of neutral atoms available to ionize and may change the harmonic power that is produced.

In light of all these drawbacks, we concluded that the most promising approach to doing DCS in the VUV was with a second independent fsEC.

5.5 Two Cavity DCS

5.5.1 Setup

The two cavity approach to DCS in the VUV/XUV is somewhat simpler conceptually as it is a direct extension of standard DCS. While there is the additional complication of a second fsEC, the chief difficulties in implementing this approach are that beam-

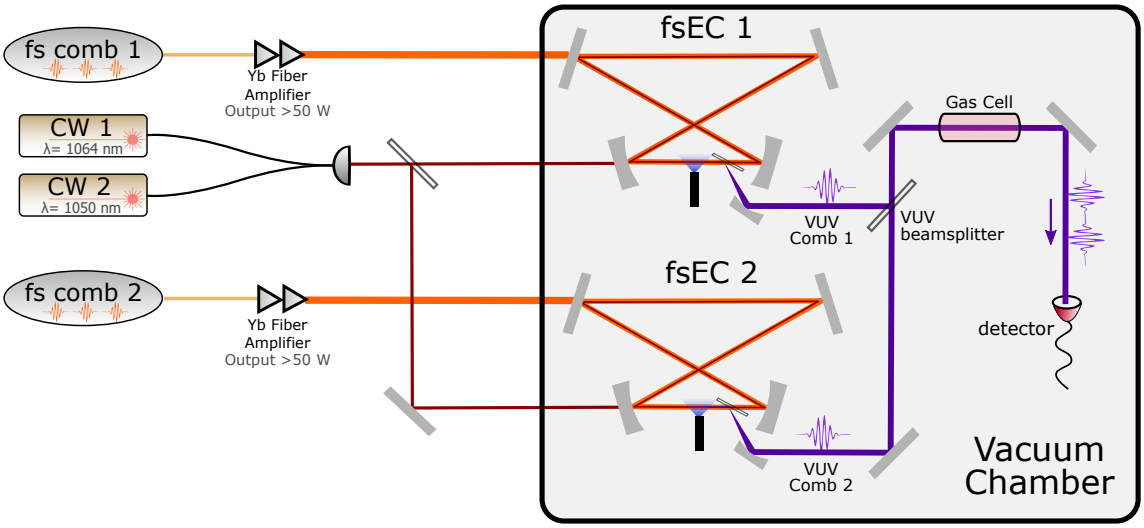

FIGURE 5.6. Simplified schematic of the dual comb VUV spectroscopy system. Two high power frequency combs seed independent fsECs to generate VUV combs. The two VUV combs are overlapped at beamsplitter and passed through a gas sample before going to the detection system.

splitters that work at VUV and XUV wavelengths are difficult to make and aligning an interferometer under vacuum conditions is very challenging. In 2014, Benko et. al demonstrated an XUV interferometer using a custom silicon beamsplitter based on a wavefront division scheme that produced interference fringes in the far field [88]. Fortunately, for applications in the VUV at 150 nm and longer wavelengths, the task is slightly easier as optically transparent beamsplitters are readily available. In this work, a CaF substrate with a dielectric coating with a reflectivity of about 35% (p-polarization) was used as a beamsplitter (Layertec 110145).

A schematic of our VUV dual comb system is shown in Figure 5.6. Alignment of the VUV interferometer still needs to be performed in a vacuum environment which requires the use of piezo-electric mirror actuators for fine adjustment. The biggest downside to these actuators for fsEC applications is that they operate at kHz frequencies and couple strong vibrations to the optical breadboard the cavity is mounted on.

This makes optimizing the alignment a tedious process because the cavity needs to be relocked with every adjustment. Having smoothly adjusting actuators would make optimization of the alignment and observed IGMs much simpler.

Our detection system for the 7th harmonic interference signal uses a VUV monochromator (McPherson Model 302, not shown in schematic) having a 2400 grooves/mm grating to achieve a resolution of 0.06 nm. A sodium salicylate coated window is placed behind the monochromator exit slit to convert the VUV light to the visible where it is then detected by a photomultiplier tube (Hamamatsu R6095).

5.5.2 Results

We have not yet been able to observe time-domain interferograms (IGMs) at the 7th harmonic. However, the 3rd harmonic provides an easier task of overlapping the beams with good signal to noise. Figure 5.7 shows an example spectrum obtained from overlapping 3rd harmonic beams from each fsEC. The overall envelope of the spectrum in the top plot corresponds to the frequency spectrum of a single time-domain IGM (shown in the inset). This is the first time a dual comb spectrum has been recorded from an IHHG system. The complete 150 ms acquisition contains about 30 total IGMs and has a transform-limited resolution of about 7 Hz in the RF. An 800x zoom of the spectrum around 15.5 MHz is shown in the lower plot and reveals the underlying comb structure with a comb line spacing equal to the repetition rate difference (Δf_{rep}) of the two lasers.

Besides the difficulty of overlapping the beams, another challenge of detecting the 7th harmonic interference signal is that amplitude noise in the fundamental cavity lock couples strongly to the powers of the harmonics and increases with harmonic order. This is a consequence of the high-order nonlinearity of the HHG process and means that minimizing noise in the cavity is vitally important to achieving a usable signal-to-noise in the 7th harmonic IGMs.

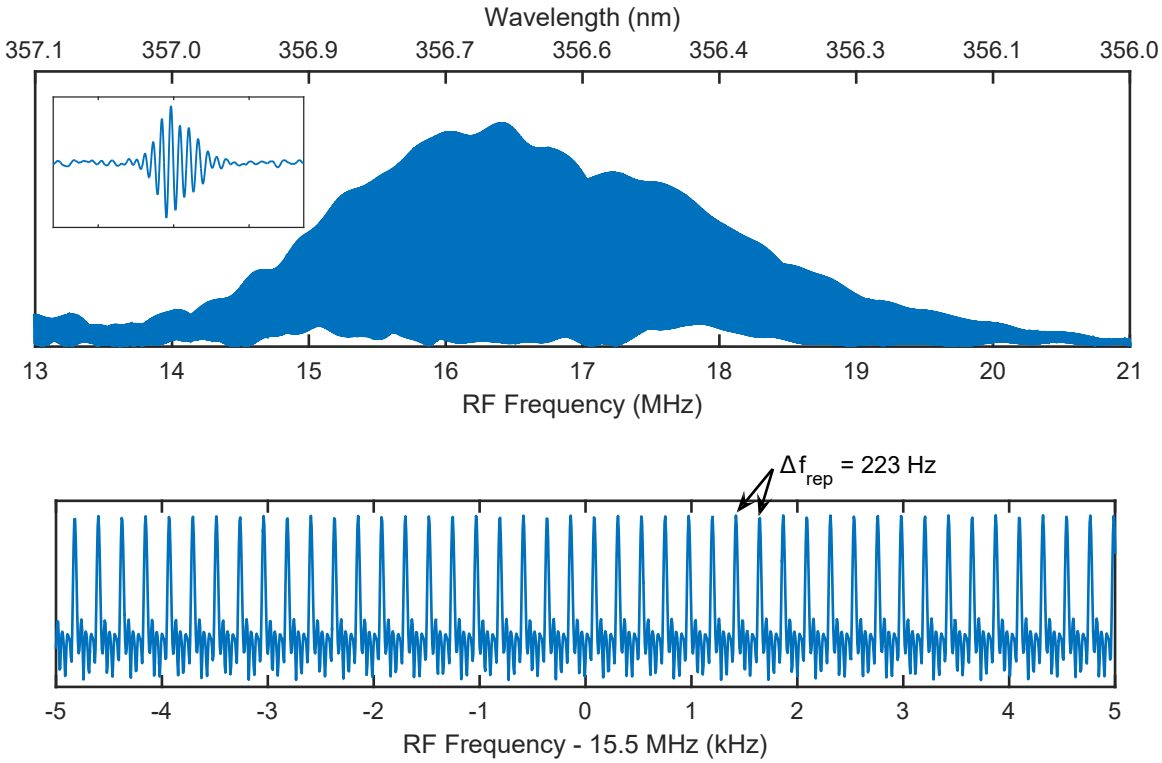

FIGURE 5.7. Sample dual comb spectrum obtained at the third harmonic of the Yb fiber laser. The top plot shows the full spectrum both in terms of optical wavelength and down-converted RF. The inset in the plot shows a single time-domain interferogram in the acquisition used to create the spectrum. The lower graph shows the spectrum zoomed in by a factor of 800 and reveals the individual comb modes spaced by the repetition rate difference $\Delta f_{\text{rep}} = 223$ Hz.

5.5.3 Outlook

A successful demonstration of a measurement of an atomic or molecular transition in the VUV using DCS will at first be limited to a small subset of possible molecular species. At present, tuning the center wavelength of the laser system is a non-trivial process involving modifying the laser oscillator and the fsEC mirror coatings. Therefore it is important that the design wavelength leads to the appropriate harmonic order overlapping with the desired molecular transition. In our system, the 7th harmonic is centered around 152 nm and is chosen to align with relatively narrow transitions in both acetylene and acetone [89, 90, 91]. Each of these molecules can be probed in a gaseous state using an absorption measurement and are probably the best candidates for an initial demonstration of the technique in the VUV.

Chapter 6

Conclusions

Since the first demonstrations of intracavity HHG, the amount of output-coupled power in the individual harmonic orders has increased by over three orders of magnitude. Limitations of early IHHG experiments related to phase matching and achievable pulse energy in the cavity have largely been overcome through the use of better cavity design and higher power laser systems. However, recent studies have shown that the intracavity plasma and optically induced damage are still limiting factors towards scaling the systems to higher power. Still, current power levels are sufficient to perform useful spectroscopic measurements and should enable new high-resolution VUV and XUV results in the near future.

In this work we performed a series of numerical simulations to investigate the IHHG limitations related specifically to the plasma that forms at the intracavity focus. Our results showed for the first time that there is a fundamental limit to the pulse enhancement that can be achieved in these systems due to the nonlinear chirp acquired by the circulating pulse. Furthermore, we established that there is a significant static background plasma that persists between cavity round-trips and it is this background plasma that causes problems with the active stabilization electronics.

By utilizing a second, independent frequency comb laser, we were able to directly measure the intracavity plasma in real-time. This pump-probe technique provided insights into the plasma decay mechanisms and provides an ideal tool for measuring ionization dynamics *in situ*.

Finally, a high power phase-coherent dual comb laser system was constructed to seed two parallel enhancement cavities for dual comb spectroscopy. Preliminary re-

sults showing interferograms and comb spectra at the third harmonic were presented. While this was not strictly a VUV comb, it represented the first comb-resolved measurement from an IHHG system. Future development of this system will yield IGMs at the 7th harmonic and enable high-resolution dual comb spectroscopy of molecular species in the VUV. This system has the potential to greatly exceed the resolution of the synchrotron based FTS experiments mentioned in Chapter 1 that currently provide the state-of-the-art measurements of atomic and molecular transitions in the VUV.

References

[1] R. Teets, J. Eckstein, and T. W. Hänsch, "Coherent Two-Photon Excitation by Multiple Light Pulses", Physical Review Letters **38**, 760 (1977).

[2] J. N. Eckstein, A. I. Ferguson, and T. W. Hänsch, "High-Resolution Two-Photon Spectroscopy with Picosecond Light Pulses", Physical Review Letters **40**, 847 (1978).

[3] T. Udem, J. Reichert, R. Holzwarth, and T. W. Hänsch, "Absolute Optical Frequency Measurement of the Cesium D1 Line with a Mode-Locked Laser", Physical Review Letters **82**, 3568 (1999).

[4] D. J. Jones, S. A. Diddams, J. K. Ranka, A. Stentz, R. S. Windeler, J. L. Hall, and S. T. Cundiff, "Carrier-Envelope Phase Control of Femtosecond Mode-Locked Lasers and Direct Optical Frequency Synthesis", Science **288**, 635 (2000).

[5] S. A. Diddams, T. Udem, J. C. Bergquist, E. A. Curtis, R. E. Drullinger, L. Hollberg, W. M. Itano, W. D. Lee, C. W. Oates, K. R. Vogel, and D. J. Wineland, "An Optical Clock Based on a Single Trapped 199Hg+ Ion", Science **293**, 825 (2001).

[6] J. Ye, L. S. Ma, and J. L. Hall, "Molecular Iodine Clock", Physical Review Letters **87**, 270801 (2001).

[7] S. A. Diddams, L. Hollberg, and V. Mbele, "Molecular fingerprinting with the resolved modes of a femtosecond laser frequency comb", Nature **445**, 627 (2007).

[8] A. Schliesser, M. Brehm, F. Keilmann, and D. W. van der Weide, "Frequency-comb infrared spectrometer for rapid, remote chemical sensing", Optics Express **13**, 9029 (2005).

[9] M. Fischer, N. Kolachevsky, M. Zimmermann, R. Holzwarth, T. Udem, T. W. Hänsch, M. Abgrall, J. Grünert, I. Maksimovic, S. Bize, H. Marion, F. P. D. Santos, P. Lemonde, G. Santarelli, P. Laurent, A. Clairon, C. Salomon, M. Haas, U. D. Jentschura, and C. H. Keitel, "New Limits on the Drift of Fundamental Constants from Laboratory Measurements", Physical Review Letters **92**, 230802 (2004).

[10] M. Golkowski, C. Golkowski, J. Leszczynski, S. Plimpton, P. Maslowski, A. Foltynowicz, J. Ye, and B. McCollister, "Hydrogen-Peroxide-Enhanced Non-thermal Plasma Effluent for Biomedical Applications", IEEE Transactions on Plasma Science **40**, 1984 (2012).

[11] M. T. Murphy, T. Udem, R. Holzwarth, A. Sizmann, L. Pasquini, C. Araujo-Hauck, H. Dekker, S. D'Odorico, M. Fischer, T. W. Hänsch, and A. Manescau, "High-precision wavelength calibration of astronomical spectrographs with laser frequency combs", Monthly Notices of the Royal Astronomical Society **380**, 839 (2007).

[12] T. Steinmetz, T. Wilken, C. Araujo-Hauck, R. Holzwarth, T. W. Hänsch, L. Pasquini, A. Manescau, S. D'Odorico, M. T. Murphy, T. Kentischer, W. Schmidt, and T. Udem, "Laser Frequency Combs for Astronomical Observations", Science **321**, 1335 (2008).

[13] A. Schliesser, N. Picqué, and T. W. Hänsch, "Mid-infrared frequency combs", Nature Photonics **6**, 440 (2012).

[14] M. Herrmann, M. Haas, U. D. Jentschura, F. Kottmann, D. Leibfried, G. Saathoff, C. Gohle, A. Ozawa, V. Batteiger, S. Knünz, N. Kolachevsky, H. A. Schüssler, T. W. Hänsch, and T. Udem, "Feasibility of coherent xuv spectroscopy on the 1S-2S transition in singly ionized helium", Physical Review A **79**, 052505 (2009).

[15] J. C. Berengut and V. V. Flambaum, "Laboratory spectroscopy and the search for variation of the fine-structure constant", Hyperfine Interactions **196**, 269 (2010).

[16] B. R. Beck, J. A. Becker, P. Beiersdorfer, G. V. Brown, K. J. Moody, J. B. Wilhelmy, F. S. Porter, C. A. Kilbourne, and R. L. Kelley, "Energy Splitting of the Ground-State Doublet in the Nucleus Th229", Physical Review Letters **98**, 142501 (2007).

[17] W. G. Rellergert, D. DeMille, R. R. Greco, M. P. Hehlen, J. R. Torgerson, and E. R. Hudson, "Constraining the Evolution of the Fundamental Constants with a Solid-State Optical Frequency Reference Based on the Th229 Nucleus", Physical Review Letters **104**, 200802 (2010).

[18] N. de Oliveira, M. Roudjane, D. Joyeux, D. Phalippou, J.-C. Rodier, and L. Nahon, "High-resolution broad-bandwidth Fourier-transform absorption spectroscopy in the VUV range down to 40 nm", Nature Photonics **5**, 149 (2011).

[19] K. Niemi, D. O'Connell, N. de Oliveira, D. Joyeux, L. Nahon, J. P. Booth, and T. Gans, "Absolute atomic oxygen and nitrogen densities in radio-frequency driven atmospheric pressure cold plasmas: Synchrotron vacuum ultra-violet high-resolution Fourier-transform absorption measurements", Applied Physics Letters **103**, 034102 (2013).

[20] D. Z. Kandula, C. Gohle, T. J. Pinkert, W. Ubachs, and K. S. E. Eikema, "Extreme Ultraviolet Frequency Comb Metrology", Physical Review Letters **105**, 063001 (2010).

[21] A. Cingöz, D. C. Yost, T. K. Allison, A. Ruehl, M. E. Fermann, I. Hartl, and J. Ye, "Direct frequency comb spectroscopy in the extreme ultraviolet", Nature **482**, 68 (2012).

[22] R. Holzwarth, T. Udem, T. W. Hänsch, J. C. Knight, W. J. Wadsworth, and P. S. J. Russell, "Optical Frequency Synthesizer for Precision Spectroscopy", Physical Review Letters **85**, 2264 (2000).

[23] R. Ell, U. Morgner, F. X. Kärtner, J. G. Fujimoto, E. P. Ippen, V. Scheuer, G. Angelow, T. Tschudi, M. J. Lederer, A. Boiko, and B. Luther-Davies, "Generation of 5-fs pulses and octave-spanning spectra directly from a Ti:sapphire laser", Optics Letters **26**, 373 (2001).

[24] A. McPherson, G. Gibson, H. Jara, U. Johann, T. S. Luk, I. A. McIntyre, K. Boyer, and C. K. Rhodes, "Studies of multiphoton production of vacuum-ultraviolet radiation in the rare gases", JOSA B **4**, 595 (1987).

[25] M. Ferray, A. L'Huillier, X. F. Li, L. A. Lompre, G. Mainfray, and C. Manus, "Multiple-harmonic conversion of 1064 nm radiation in rare gases", Journal of Physics B: Atomic, Molecular and Optical Physics **21**, L31 (1988).

[26] M. Hentschel, R. Kienberger, C. Spielmann, G. A. Reider, N. Milosevic, T. Brabec, P. Corkum, U. Heinzmann, M. Drescher, and F. Krausz, "Attosecond metrology", Nature **414**, 509 (2001).

[27] L. V. Keldysh, "Ionization in the field of a strong electromagnetic wave", Sov. Phys. JETP **20**, 1307 (1965).

[28] J. L. Krause, K. J. Schafer, and K. C. Kulander, "High-order harmonic generation from atoms and ions in the high intensity regime", Physical Review Letters **68**, 3535 (1992).

[29] P. B. Corkum, "Plasma perspective on strong field multiphoton ionization", Physical Review Letters **71**, 1994 (1993).

[30] M. Lewenstein, P. Balcou, M. Y. Ivanov, A. L'Huillier, and P. B. Corkum, "Theory of high-harmonic generation by low-frequency laser fields", Physical Review A **49**, 2117 (1994).

[31] A. Rundquist, C. G. Durfee, Z. Chang, C. Herne, S. Backus, M. M. Murnane, and H. C. Kapteyn, "Phase-Matched Generation of Coherent Soft X-rays", Science **280**, 1412 (1998).

[32] P. Balcou, P. Sali'eres, A. L'Huillier, and M. Lewenstein, "Generalized phase-matching conditions for high harmonics: The role of field-gradient forces", Physical Review A **55**, 3204 (1997).

[33] E. Constant, D. Garzella, P. Breger, E. Mével, C. Dorrer, C. Le Blanc, F. Salin, and P. Agostini, "Optimizing High Harmonic Generation in Absorbing Gases: Model and Experiment", Physical Review Letters **82**, 1668 (1999).

[34] A. Paul, R. A. Bartels, R. Tobey, H. Green, S. Weiman, I. P. Christov, M. M. Murnane, H. C. Kapteyn, and S. Backus, "Quasi-phase-matched generation of coherent extreme-ultraviolet light", Nature **421**, 51 (2003).

[35] C. Spielmann, N. H. Burnett, S. Sartania, R. Koppitsch, M. Schnürer, C. Kan, M. Lenzner, P. Wobrauschek, and F. Krausz, "Generation of Coherent X-rays in the Water Window Using 5-Femtosecond Laser Pulses", Science **278**, 661 (1997).

[36] A. Baltuška, T. Udem, M. Uiberacker, M. Hentschel, E. Goulielmakis, C. Gohle, R. Holzwarth, V. S. Yakovlev, A. Scrinzi, T. W. Hänsch, and F. Krausz, "Attosecond control of electronic processes by intense light fields", Nature **421**, 611 (2003).

[37] T. Popmintchev, M.-C. Chen, D. Popmintchev, P. Arpin, S. Brown, S. Ališauskas, G. Andriukaitis, T. Balčiunas, O. D. Mücke, A. Pugzlys, A. Baltuška, B. Shim, S. E. Schrauth, A. Gaeta, C. Hernández-García, L. Plaja,

A. Becker, A. Jaron-Becker, M. M. Murnane, and H. C. Kapteyn, "Bright Coherent Ultrahigh Harmonics in the keV X-ray Regime from Mid-Infrared Femtosecond Lasers", Science **336**, 1287 (2012).

[38] A. Vernaleken, J. Weitenberg, T. Sartorius, P. Russbueldt, W. Schneider, S. L. Stebbings, M. F. Kling, P. Hommelhoff, H.-D. Hoffmann, R. Poprawe, F. Krausz, T. W. Hänsch, and T. Udem, "Single-pass high-harmonic generation at 20.8 MHz repetition rate", Optics Letters **36**, 3428 (2011).

[39] R. J. Jones, K. D. Moll, M. J. Thorpe, and J. Ye, "Phase-Coherent Frequency Combs in the Vacuum Ultraviolet via High-Harmonic Generation inside a Femtosecond Enhancement Cavity", Physical Review Letters **94**, 193201 (2005).

[40] C. Gohle, T. Udem, M. Herrmann, J. Rauschenberger, R. Holzwarth, H. A. Schuessler, F. Krausz, and T. W. Hänsch, "A frequency comb in the extreme ultraviolet", Nature **436**, 234 (2005).

[41] J. Lee, D. R. Carlson, and R. J. Jones, "Optimizing intracavity high harmonic generation for XUV fs frequency combs", Optics Express **19**, 23315 (2011).

[42] H. Carstens, M. Högner, T. Saule, S. Holzberger, N. Lilienfein, A. Guggenmos, C. Jocher, T. Eidam, D. Esser, V. Tosa, V. Pervak, J. Limpert, A. Tünnermann, U. Kleineberg, F. Krausz, and I. Pupeza, "High-harmonic generation at 250 MHz with photon energies exceeding 100 eV", Optica **3**, 366 (2016).

[43] A. E. Siegman, *Lasers* (University Science Books, Mill Valley, Calif., 1986).

[44] D. C. Yost, T. R. Schibli, and J. Ye, "Efficient output coupling of intracavity high-harmonic generation", Optics Letters **33**, 1099 (2008).

[45] Y.-Y. Yang, F. Süßmann, S. Zherebtsov, I. Pupeza, J. Kaster, D. Lehr, H.-J. Fuchs, E.-B. Kley, E. Fill, X.-M. Duan, Z.-S. Zhao, F. Krausz, S. L. Stebbings,

and M. F. Kling, "Optimization and characterization of a highly-efficient diffraction nanograting for MHz XUV pulses", Optics Express **19**, 1954 (2011).

[46] K. D. Moll, R. J. Jones, and J. Ye, "Output coupling methods for cavity-based high-harmonic generation", Optics Express **14**, 8189 (2006).

[47] J. Weitenberg, P. Rußbüldt, T. Eidam, and I. Pupeza, "Transverse mode tailoring in a quasi-imaging high-finesse femtosecond enhancement cavity", Optics Express **19**, 9551 (2011).

[48] I. Pupeza, S. Holzberger, T. Eidam, H. Carstens, D. Esser, J. Weitenberg, P. Rußbüldt, J. Rauschenberger, J. Limpert, T. Udem, A. Tünnermann, T. W. Hänsch, A. Apolonski, F. Krausz, and E. Fill, "Compact high-repetition-rate source of coherent 100 eV radiation", Nature Photonics **7**, 608 (2013).

[49] A. Ozawa, J. Rauschenberger, C. Gohle, M. Herrmann, D. R. Walker, V. Pervak, A. Fernandez, R. Graf, A. Apolonski, R. Holzwarth, F. Krausz, T. W. Hänsch, and T. Udem, "High Harmonic Frequency Combs for High Resolution Spectroscopy", Physical Review Letters **100**, 253901 (2008).

[50] M. Louisy, C. L. Arnold, M. Miranda, E. W. Larsen, S. N. Bengtsson, D. Kroon, M. Kotur, D. Guénot, L. Rading, P. Rudawski, F. Brizuela, F. Campi, B. Kim, A. Jarnac, A. Houard, J. Mauritsson, P. Johnsson, A. L'Huillier, and C. M. Heyl, "Gating attosecond pulses in a noncollinear geometry", Optica **2**, 563 (2015).

[51] O. Pronin, V. Pervak, E. Fill, J. Rauschenberger, F. Krausz, and A. Apolonski, "Ultrabroadband efficient intracavity XUV output coupler", Optics Express **19**, 10232 (2011).

[52] I. Pupeza, E. E. Fill, and F. Krausz, "Low-loss VIS/IR-XUV beam splitter for high-power applications", Optics Express **19**, 12108 (2011).

[53] T. C. Briles, D. C. Yost, J. Ye, T. R. Schibli, and others, "Simple piezoelectric-actuated mirror with 180 kHz servo bandwidth", Optics Express **18**, 9739 (2010).

[54] R. W. P. Drever, J. L. Hall, F. V. Kowalski, J. Hough, G. M. Ford, A. J. Munley, and H. Ward, "Laser phase and frequency stabilization using an optical resonator", Applied Physics B **31**, 97 (1983).

[55] R. J. Jones, J.-C. Diels, J. Jasapara, and W. Rudolph, "Stabilization of the frequency, phase, and repetition rate of an ultra-short pulse train to a Fabry–Perot reference cavity", Optics Communications **175**, 409 (2000).

[56] S. Holzberger, N. Lilienfein, M. Trubetskov, H. Carstens, F. Lücking, V. Pervak, F. Krausz, and I. Pupeza, "Enhancement cavities for zero-offset-frequency pulse trains", Optics Letters **40**, 2165 (2015).

[57] I. Pupeza, T. Eidam, J. Rauschenberger, B. Bernhardt, A. Ozawa, E. Fill, A. Apolonski, T. Udem, J. Limpert, Z. A. Alahmed, A. M. Azzeer, A. Tünnermann, T. W. Hänsch, and F. Krausz, "Power scaling of a high-repetition-rate enhancement cavity", Optics Letters **35**, 2052 (2010).

[58] J. Hollenshead and L. Klebanoff, "Modeling radiation-induced carbon contamination of extreme ultraviolet optics", Journal of Vacuum Science & Technology B **24**, 64 (2006).

[59] A. Pereira, E. Quesnel, and M. Reymermier, "Dynamic measurements of ultraviolet-enhanced silica contamination by photoluminescence-based diagnostic", Journal of Applied Physics **105**, 013109 (2009).

[60] A. K. Mills, T. J. Hammond, M. H. C. Lam, and D. J. Jones, "XUV frequency combs via femtosecond enhancement cavities", Journal of Physics B: Atomic, Molecular and Optical Physics **45**, 142001 (2012).

[61] H. Carstens, S. Holzberger, J. Kaster, J. Weitenberg, V. Pervak, A. Apolonski, E. Fill, F. Krausz, and I. Pupeza, "Large-mode enhancement cavities", Optics Express **21**, 11606 (2013).

[62] J. Paul, J. Johnson, J. Lee, and R. J. Jones, "Generation of high-power frequency combs from injection-locked femtosecond amplification cavities", Optics Letters **33**, 2482 (2008).

[63] B. Bernhardt, A. Ozawa, A. Vernaleken, I. Pupeza, J. Kaster, Y. Kobayashi, R. Holzwarth, E. Fill, F. Krausz, T. W. Hänsch, and T. Udem, "Vacuum ultraviolet frequency combs generated by a femtosecond enhancement cavity in the visible", Optics Letters **37**, 503 (2012).

[64] V. J. Matsas, T. P. Newson, D. J. Richardson, and D. N. Payne, "Selfstarting passively mode-locked fibre ring soliton laser exploiting nonlinear polarisation rotation", Electronics Letters **28**, 1391 (1992).

[65] M. E. Fermann, M. L. Stock, M. J. Andrejco, and Y. Silberberg, "Passive mode locking by using nonlinear polarization evolution in a polarization-maintaining erbium-doped fiber", Optics Letters **18**, 894 (1993).

[66] M. E. Fermann, V. I. Kruglov, B. C. Thomsen, J. M. Dudley, and J. D. Harvey, "Self-Similar Propagation and Amplification of Parabolic Pulses in Optical Fibers", Physical Review Letters **84**, 6010 (2000).

[67] D. N. Papadopoulos, Y. Zaouter, M. Hanna, F. Druon, E. Mottay, E. Cormier, and P. Georges, "Generation of 63 fs 4.1 MW peak power pulses from a parabolic fiber amplifier operated beyond the gain bandwidth limit", Optics Letters **32**, 2520 (2007).

[68] A. M. Perelomov, V. S. Popov, and M. V. Terent'ev, "Ionization of atoms in an alternating electric field", Sov. Phys. JETP **23**, 924 (1966).

[69] T. J. Hammond, *Intracavity Generation of High Order Harmonics*, Ph.D. thesis, University of British Columbia (2011).

[70] T. K. Allison, A. Cingöz, D. C. Yost, and J. Ye, "Extreme Nonlinear Optics in a Femtosecond Enhancement Cavity", Physical Review Letters **107**, 183903 (2011).

[71] F. F. Chen, *Introduction to Plasma Physics and Controlled Fusion* (Springer US, Boston, MA, 1984).

[72] D. R. Carlson, J. Lee, J. Mongelli, E. M. Wright, and R. J. Jones, "Intracavity ionization and pulse formation in femtosecond enhancement cavities", Optics Letters **36**, 2991 (2011).

[73] J. Mongelli, *Temporal Optical Soliton Dynamics in Femtosecond Enhancement Cavities*, Master's thesis, University of Arizona (2012).

[74] D. R. Carlson, J. Mongelli, E. M. Wright, and R. J. Jones, in *Proc. SPIE 8132, Time and Frequency Metrology III* (SPIE, 2011), p. 813205.

[75] A. Cutolo, P. Gay, and S. Solimeno, "Mirror Deformations and Wavefront Aberrations Caused by C.w. High Power Laser Beams", Optica Acta: International Journal of Optics **27**, 1105 (1980).

[76] P. Jacquinot, "New developments in interference spectroscopy", Reports on Progress in Physics **23**, 267 (1960).

[77] P. Griffiths and J. De Haseth, *Fourier Transform Infrared Spectrometry*, Chemical Analysis: A Series of Monographs on Analytical Chemistry and Its Applications (Wiley, 2007).

[78] S. Schiller, "Spectrometry with frequency combs", Optics Letters **27**, 766 (2002).

[79] F. Keilmann, C. Gohle, and R. Holzwarth, "Time-domain mid-infrared frequency-comb spectrometer", Optics Letters **29**, 1542 (2004).

[80] I. Coddington, W. Swann, and N. Newbury, "Coherent Multiheterodyne Spectroscopy Using Stabilized Optical Frequency Combs", Physical Review Letters **100** (2008).

[81] A. Hipke, S. A. Meek, G. Guelachvili, T. W. Hänsch, and N. Picque, in *CLEO: 2013 Postdeadline* (Optical Society of America, 2013), p. CTh5C.8.

[82] P. Giaccari, J.-D. Deschênes, P. Saucier, J. Genest, and P. Tremblay, "Active Fourier-transform spectroscopy combining the direct RF beating of two fiber-based mode-locked lasers with a novel referencing method", Optics Express **16**, 4347 (2008).

[83] J.-D. Deschênes, P. Giaccarri, J. Genest, and others, "Optical referencing technique with CW lasers as intermediate oscillators for continuous full delay range frequency comb interferometry", Optics Express **18**, 23358 (2010).

[84] T. Ideguchi, A. Poisson, G. Guelachvili, T. W. Hänsch, and N. Picqué, "Adaptive dual-comb spectroscopy in the green region", Optics Letters **37**, 4847 (2012).

[85] T. Ideguchi, A. Poisson, G. Guelachvili, N. Picqué, and T. W. Hänsch, "Adaptive real-time dual-comb spectroscopy", Nature Communications **5** (2014).

[86] V. Blanchet, C. Nicole, M.-A. Bouchene, and B. Girard, "Temporal Coherent Control in Two-Photon Transitions: From Optical Interferences to Quantum Interferences", Physical Review Letters **78**, 2716 (1997).

[87] M. A. Bouchene, C. Nicole, and B. Girard, "Interplay between wave packet interferences and second harmonic generation", Optics Communications **181**, 327 (2000).

[88] C. Benko, T. K. Allison, A. Cingöz, L. Hua, F. Labaye, D. C. Yost, and J. Ye, "Extreme ultraviolet radiation with coherence time greater than 1 s", Nature Photonics **8**, 530 (2014).

[89] P. L. Smith, K. Yoshino, W. H. Parkinson, K. Ito, and G. Stark, "High-resolution, VUV (147–201 nm) photoabsorption cross sections for C2H2 at 195 and 295 K", Journal of Geophysical Research: Planets **96**, 17529 (1991).

[90] M. Nobre, A. Fernandes, F. F. da Silva, R. Antunes, D. Almeida, V. Kokhan, S. V. Hoffmann, N. J. Mason, S. Eden, and P. Limão-Vieira, "The VUV electronic spectroscopy of acetone studied by synchrotron radiation", Physical Chemistry Chemical Physics **10**, 550 (2008).

[91] B.-M. Cheng, H.-F. Chen, H.-C. Lu, H.-K. Chen, M. S. Alam, S.-L. Chou, and M.-Y. Lin, "Absorption Cross Section of Gaseous Acetylene at 85 K in the Wavelength Range 110-155 nm", The Astrophysical Journal Supplement Series **196**, 3 (2011).